Journal of the Mechanics and Physics of Solids 137 (2020) 103843

Contents lists available at ScienceDirect

Journal of the Mechanics and Physics of Solids

journal homepage: www.elsevier.com/locate/jmps

# Radial buckle delamination around 2D material tents

Zhaohe Dai [a], Daniel A. Sanchez [b], Christopher J. Brennan [c,d], Nanshu Lu [a,b,d,*]

[a] Center for Mechanics of Solids, Structures and Materials, Department of Aerospace Engineering and Engineering Mechanics, The University of Texas at Austin, Austin, Texas 78712, USA
[b] Texas Materials Institute, The University of Texas at Austin, Austin, Texas 78712, USA
[c] Microelectronics Research Center, The University of Texas at Austin, Austin, Texas, 78758, USA
[d] Department of Electrical and Computer Engineering, The University of Texas at Austin, Austin, Texas, 78701, USA

ARTICLE INFO

*Article history:*
Received 31 May 2019
Revised 27 October 2019
Accepted 17 December 2019
Available online 11 January 2020

ABSTRACT

Microscale tents, formed when transferring two-dimensional (2D) materials over nanoparticles or nanopillars, or when indenting a suspended 2D material drumhead with an atomic force microscope (AFM) tip, emerge to be a useful structure for the strain engineering of 2D materials. In the periphery of the tents, where the 2D materials are supported by the substrate, radial buckle delamination can often be observed, yet the formation mechanism and the profile characteristics remain unclear. Here, we suggest that the tent-induced buckles result from the 2D material-substrate interface sliding radially inward, and their profiles and extent are controlled by the interface adhesion and friction. We experimentally characterized that the crest curvature of the buckles is proportional to a characteristic length that compares the elastic bending energy of the 2D material with its adhesion energy to the substrate. We then obtain theoretical predictions for the extent of those buckles by exact closed-form solutions to Föppl–von Kármán (FvK) equations under both near-threshold and far-from-threshold conditions. Our results are highly analytical, provide a direct means to estimate the interfacial shear and adhesive properties of the 2D material-substrate system based on simple topological characterizations of buckles. Our theoretical understandings also establish a fundamental base for the rational design of 2D material tents.



## 1. Introduction

Two-dimensional (2D) materials are a relatively new class of atomically thin materials with emerging mechanical and electronic properties that lend well to next-generation nanoelectronics and nanophotonics (Geim and Grigorieva, 2013; Neto et al., 2009). Applications in this context typically involve transferring 2D materials to a supporting substrate. When 2D materials are transferred over nanoparticles on the substrate, nanotents are formed. Initially, these tents were viewed as disruptions for device applications (Akinwande et al., 2014; Pizzocchero et al., 2016). However, recent works discovered considerable mechanical strain within the tent, which is useful for many exciting electromechanical applications of 2D materials (Chaste et al., 2018; Dai et al., 2018; Dai et al., 2019a; Feng et al., 2012; Klimov et al., 2012; Tomori et al., 2011). As a result, microscale tents were designedly created by transferring 2D materials to substrates pre-patterned with nanopillars (Fig. 1a)

* Corresponding author at: Center for Mechanics of Solids, Structures and Materials, Department of Aerospace Engineering and Engineering Mechanics, The University of Texas at Austin, Austin, Texas 78712, USA.
*E-mail address:* nanshulu@utexas.edu (N. Lu).

https://doi.org/10.1016/j.jmps.2019.103843
0022-5096/

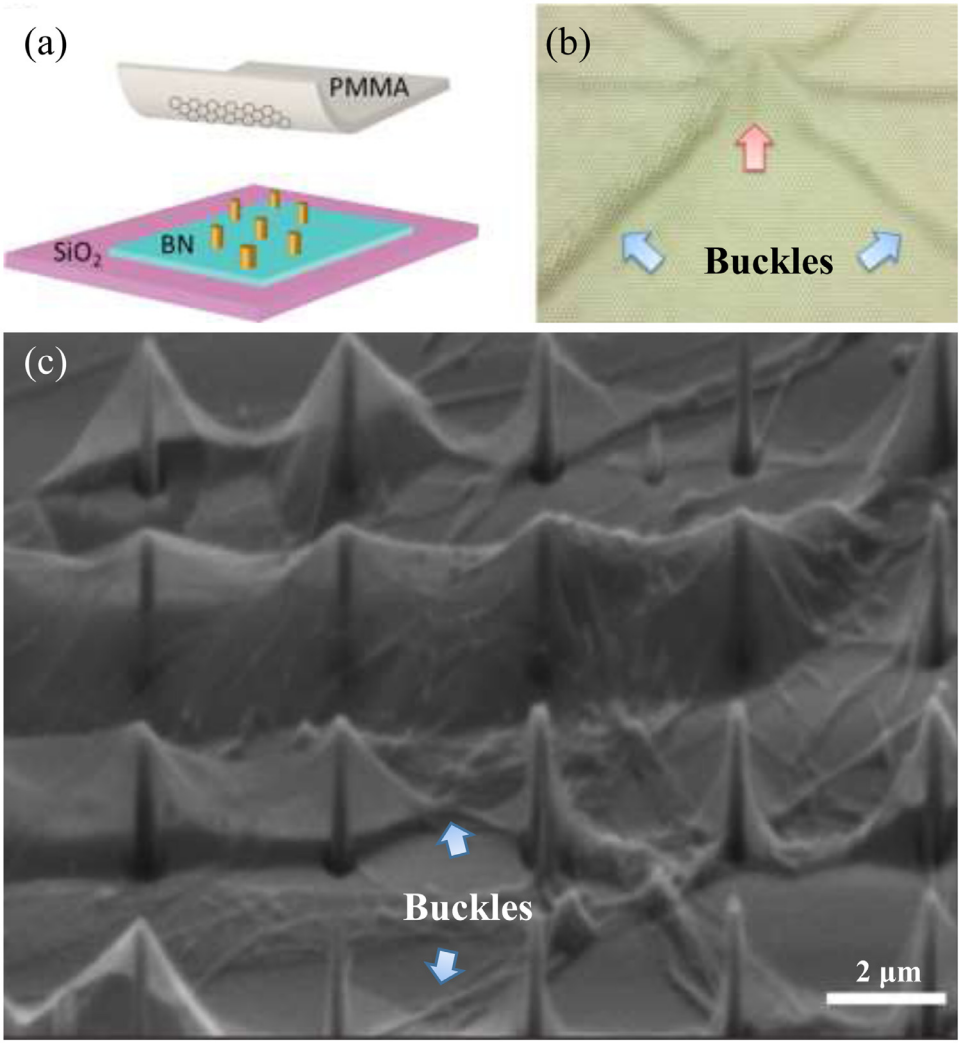


**Fig. 1.** (a) A schematic of transferring graphene over a pillared substrate. (b) A schematic of radial buckles (blue arrows) surrounding a graphene tent formed over a Au pillar (red arrow). (c) Scanning electron microscope (SEM) image of monolayer graphene covering a periodic array of nanopillars. Each nanopillar has a height of about 260 nm and an apex radius of 20 nm – 50 nm. The pillar pitch is 1.4 $\mu$m. Source: Figures adapted from (a and b) (Jiang et al., 2017) and (c) (Reserbat-Plantey et al., 2014).

(Branny et al., 2017; Jiang et al., 2017; Li et al., 2015). For example, 2D semiconductors draping over an array of nanopillars were demonstrated with the possibility to become large-scale quantum emitters, except that sometimes the pillars pierce through the 2D materials without mechanically guided design (Branny et al., 2017; Palacios-Berraquero et al. 2017). Moreover, the nanoindentation of 2D material drumheads also represents a common type of inverse 2D material tents (Cao and Gao, 2019; Lee et al., 2008). Both types of tents have been approximately modeled as circular membranes subjected to a point load at the center and clamped at the edge (Dai et al., 2019b; Komaragiri et al., 2005; Lee et al., 2008; Vella and Davidovitch, 2017). Such modeling, together with experiments on these 2D materials tents of different origins, has facilitated many vital metrologies for 2D materials, such as in-plane stiffness, mechanical strength, and adhesion energies to the substrate.

So far, both experimental and theoretical studies of 2D material tents assume that the 2D material perfectly conforms to the substrate outside the tent. However, radial buckle delamination has been widely observable in the substrate-supported zone (Fig. 1) (Jiang et al., 2017; Reserbat-Plantey et al., 2014; Zhang and Arroyo, 2016), which is prohibited under such assumption. Since the buckles can reflect 2D material-substrate interfacial interactions and affect device design, it is crucial to achieve a comprehensive mechanistic understanding for them. In this paper, we characterize radial buckles that form at the periphery of multilayer graphene and monolayer $MoS_2$ tents. Using atomic force microscopy (AFM), we find that the buckle profiles along the hoop direction follow a simple cosine function, and the wavelength and height of the buckles are proportional to a characteristic length. We attribute the radial buckles to the interface sliding between the 2D material and

its substrate. A simplified 1D analysis, along with the Lamé problem, can quantitatively explain the decay of the wavelength and the height of the buckle profile with the increasing radial position. Finally, we present theory built upon the membrane limit of Föppl–von Kármán (FvK) equations and account for the interfacial sliding in the periphery of the 2D material tents. These results show important implications for the adhesion and friction metrology of 2D materials as well as for the rational design of 2D material tents.

## 2. Experimental methods

To obtain accurate profiles of the radial buckles, we experimentally produced graphene and $MoS_2$ tents as graphene and $MoS_2$ are two of the most prevalent 2D materials studied in recent years. We prepared graphene samples by exfoliating SPI-1 grade highly ordered pyrolytic graphite (HOPG) on $SiO_2$. Blue polyethylene cleanroom tape (CRT) was used to peel large and thick flakes off the bulk crystal. The exfoliated flakes were brought into contact with another piece of the CRT and exfoliated three more times. The flakes were then stored for a minimum of three hours in ambient conditions to allow ambient moisture and other contents to adsorb on the surface of the exposed flakes. The $SiO_2$ chip was exposed to $O_2$ plasma using a Nordson MARCH Plasma CS170IF Etching System for two minutes at 150 W to remove any organic residue. Immediately after $O_2$ plasma exposure, the exfoliated HOPG flakes on CRT were placed onto the surface of the $SiO_2$ chip. Then the $SiO_2$ chip was placed on a hot plate and was heated at 100°C for two minutes. The sample was removed from the hot plate and cooled to room temperature, after which the CRT was removed. AFM step height measurement suggested that the multilayer graphene sample contained 10-20 layers, as this method is known to be inaccurate for determining 2D material thickness (Brennan et al., 2015).

We prepared monolayer $MoS_2$ by chemical vapor deposition (CVD) on $SiO_2$ from solid precursors (Brennan et al., 2017). A polydimethylsiloxane (PDMS) stamp and a water bath were used to separate the $MoS_2$ from the growth substrate. The PDMS/$MoS_2$ was then placed on the receiving substrate, $Al_2O_3$/Si, and heated with a hot plate to 50°C. Slowly peeling away the PDMS transferred the $MoS_2$ to the substrate.

We found that tents spontaneously formed when HOPG was mechanically exfoliated onto $SiO_2$ (left panel in Fig. 2a), and when CVD-grown monolayer $MoS_2$ was transferred to $Al_2O_3$ (right panel in Fig. 2a). Similar tents were also observed in many 2D material devices in the literature (Budrikis et al., 2015; Jiang et al., 2017; Reserbat-Plantey et al., 2014). The formation of tents is typically attributed to nanostructures or nanoparticles confined at the interface. In this work, we focus on the radial buckles that commonly formed at the periphery of the 2D material tents (Fig. 2a), which have been overlooked in previous experimental characterizations and theoretical analysis. We note that the substrates used here are relatively stiff as Young's moduli of silicon dioxide (supporting the multilayer graphene) and aluminum oxide (supporting the monolayer $MoS_2$) are around 70 GPa and 300 GPa, respectively.

## 3. Experiments

### 3.1. The shape of radial buckles

Using tapping mode AFM, we obtained the height images of a multilayer graphene tent and a monolayer $MoS_2$ tent as well as the radial buckles surrounding them (Fig. 2a). From these images, we extracted the height profile of a buckle by scanning transversely to the buckle (i.e. along the circumferential direction). Though depending on the radial position, i.e., the distance to the center of the tent $r$, all buckle profiles in the hoop direction could be well approximated by a cosine function (Fig. 2b),

$$y(x) = \frac{\delta}{2}\left(1 + \cos\frac{2\pi x}{\lambda}\right) \tag{1}$$

where $\lambda$ and $\delta$ are the wavelength and height of the buckle, respectively. In fact, a column undergoing Euler buckling would deflect into a shape also characterized by Eq. (1) (Timoshenko and Gere, 2009). It has been well studied that the profile of a buckle could be modified by the deformation of a soft substrate at the edge of the buckle (Audoly and Boudaoud, 2008; Boijoux et al., 2018; Parry et al., 2005). The substrates (silicon dioxide and aluminum oxide) used here, however, are relatively stiff in comparison with the bending stiffness of the 2D material flakes, and hence render the good approximation of Eq. (1).

Using Eq. (1) to fit the measured buckle profiles can readily yield $\lambda$ and $\delta$ (Vella et al., 2009). We find that both $\lambda$ and $\delta$ decay over $r$, and finally disappear at a finite distance from the center of the tent, reminiscent of the finite wrinkling zone of a water-supported elastic membrane (Huang et al., 2007; Vella et al., 2010). Fig. 2c plots experimentally measured buckle wavelength as a function of the buckle height. The power-law fitting reveals that $\lambda$ is proportional to $\sqrt{\delta}$, with a different prefactor for the multilayer graphene and the monolayer $MoS_2$. Physically, $\lambda^2/\delta$ represents the radius of curvature of the buckle's crest in the hoop direction (Aoyanagi et al., 2010; Zhang and Yin, 2018). Constant $\lambda^2/\delta$ implies that the profiles of buckles measured at different locations are self-similar as long as they are associated with the same tent. This observation suggests that each transverse scan of the buckles may be considered as an isolated one-dimensional (1D) buckle.

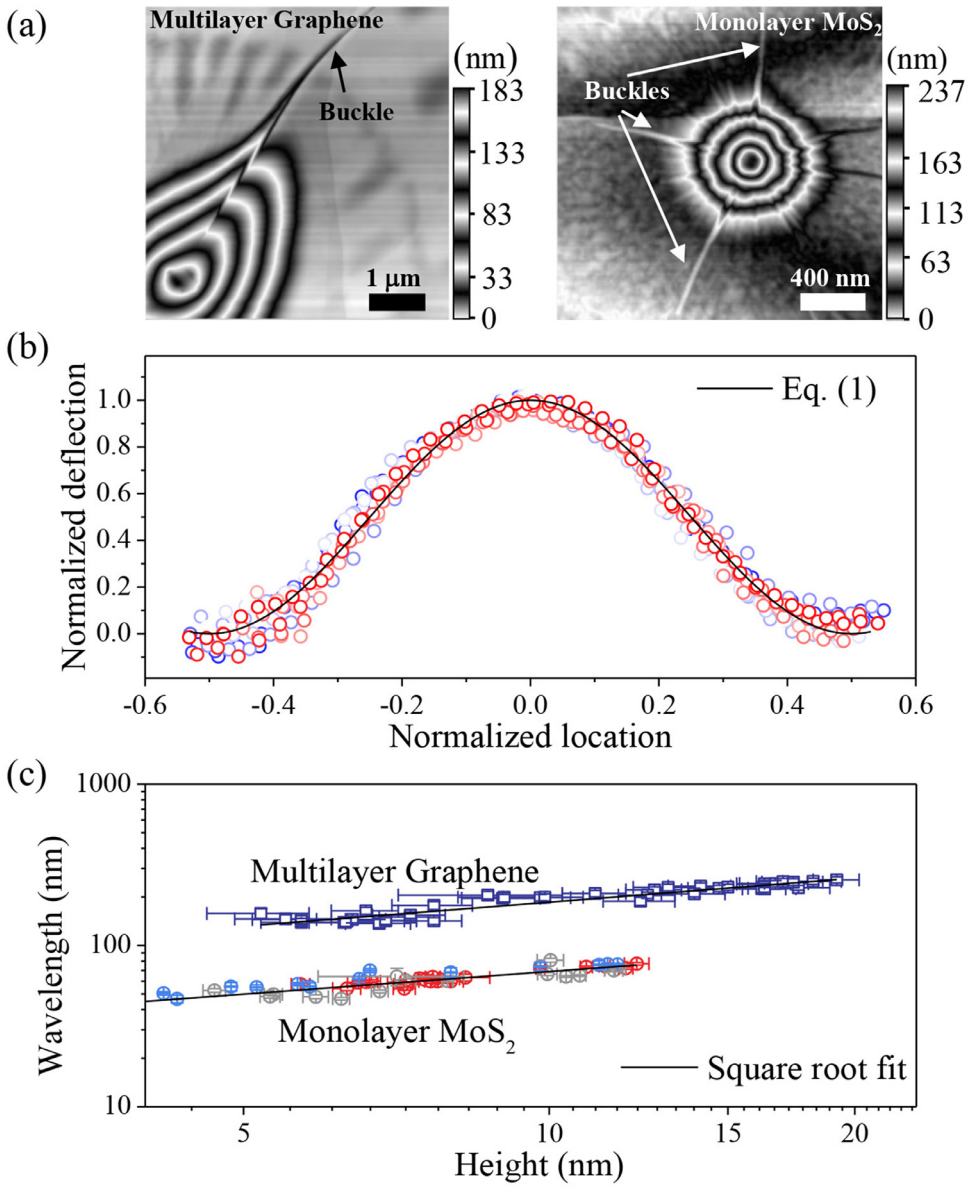


**Fig. 2.** (a) AFM images of a multilayer graphene tent and a monolayer $MoS_2$ tent. The vertical scales indicate the height of the tents. Radial buckles can be found at the substrate-supported regime outside the tent, and their profiles can be obtained by taking scans transverse to the buckles in the AFM height image. (b) Normalizing these AFM scans gives the characteristic buckle profile, which is well fitted by the cosine function given by Eq. (1) (black curve). This fit can yield the buckle wavelength $\lambda$ and height $\delta$. Different colors of the markers represent scans at different radial locations in the $MoS_2$ tent while these profiles are normalized by their fitted wavelength and height. (c) The wavelength ($\lambda$) of the multilayer graphene and monolayer $MoS_2$ buckles as a function of their height ($\delta$) in a log-log plot. Colored markers are used to differentiate different buckles surrounding the same tent. The black lines correspond to a power-law fit with an exponent of ½.

### *3.2. 1D analysis*

We recall the case of 1D buckling, where an elastic membrane buckles when subject to a uniaxial, end-to-end compressive displacement $\Delta$ (Fig. 3a). We limit ourselves to the inextensional analysis and neglect any compression of the relatively stiff thin membrane (Vella et al., 2009). The elastic energy of the system, therefore, comes from the bending of the 2D material

$$U = \frac{1}{2}B\int_{-\lambda/2}^{\lambda/2} y''(x)^2 dx = \frac{\pi^4 B\delta^2}{\lambda^3}, \tag{2}$$

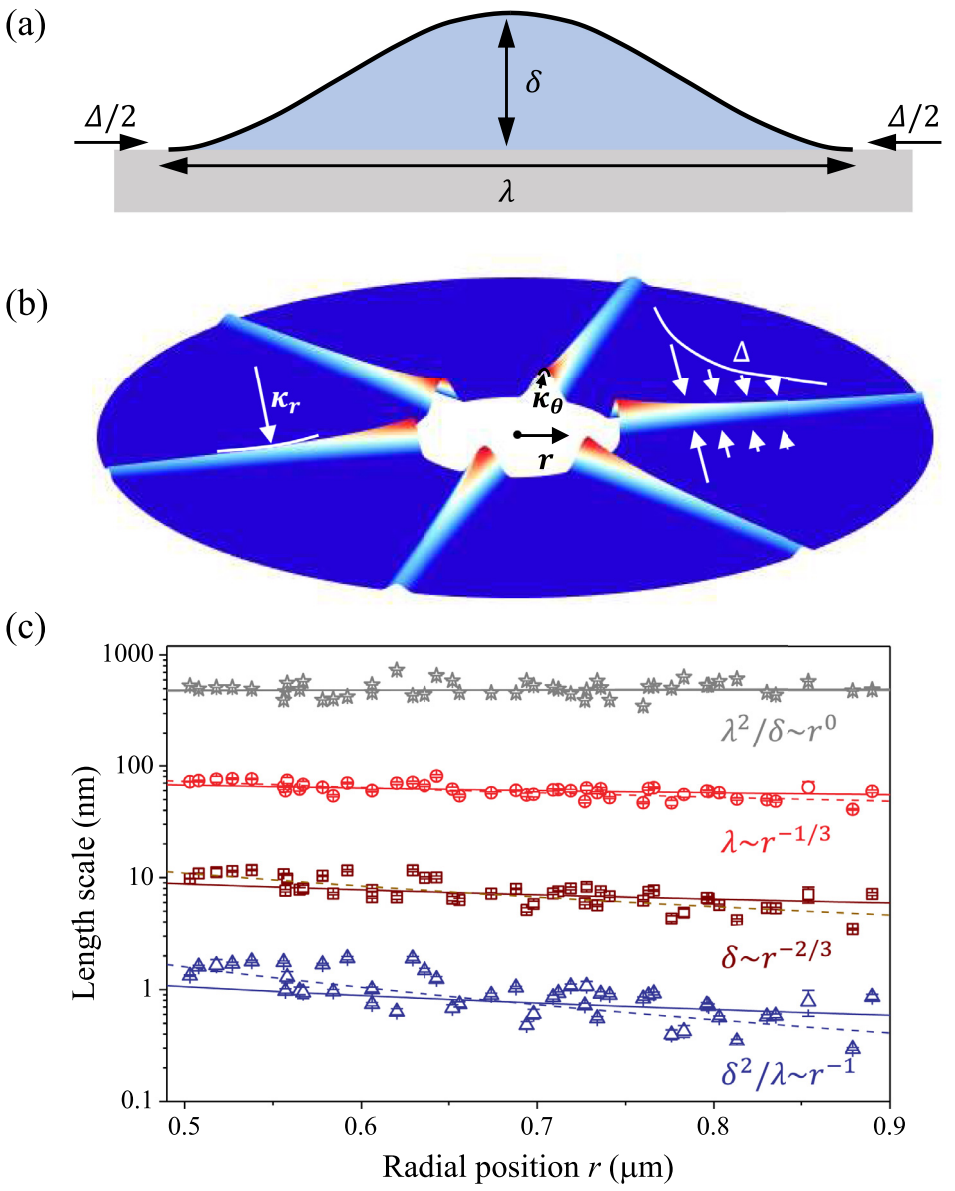


**Fig. 3.** (a) A schematic of a 1D buckle where $\Delta$ represents the compressive displacement. (b) Schematic illustration of radial buckles at the periphery of a tent. $r$ represents the radial position. $\kappa_\theta$ and $\kappa_r$ denote the buckle crest curvature in the hoop and radial direction, respectively. $\Delta$ represents the compressive displacement in the hoop direction which varies with $r$. (c) Experimentally measured $\delta^2/\lambda$, $\lambda^2/\delta$, $\lambda$, $\delta$ of the buckles formed by the monolayer $MoS_2$ tent as a function of the radial position. Solid lines are based on the scaling law given in Eq. (7), and the dashed lines represent the best fitting.

where $B$ is the bending stiffness of the membrane and $y''(x)$ is the second derivative with respect to $x$ of the tent profile given in Eq. (1), i.e. the curvature. The inextension of the membrane dictates the following geometrical relationship

$$\Delta = \int_{-\lambda/2}^{\lambda/2} \sqrt{1 + y'(x)^2}\, dx - \lambda = \frac{\pi^4 \delta^2}{4\lambda}, \tag{3}$$

which may be used to eliminate $\delta$ from Eq. (2) in favor of $\Delta$. Through $-\partial U/\partial\lambda = \Delta\gamma$, we obtain the following energy release rate

$$\Delta\gamma = 2\pi^4 \frac{B\delta^2}{\lambda^4}. \tag{4}$$

This result is identical to the previously reported macro/microscopic 1D buckles (Deng et al., 2017). However, we should be careful with the change of interfacial energy. When the delaminated interface is filled with gas, $\Delta\gamma$ is simply the adhe-

sion energy between the membrane and the substrate

$$\Delta\gamma_{\text{gas}} = \Gamma. \tag{5}$$

However, recent works showed strong evidences that the 2D material-substrate interface can spontaneously confine hydrocarbons and liquid water (Haigh et al., 2012; Khestanova et al., 2016; Sanchez et al., 2018). When the delaminated interface is filled with liquid content, the formation of a buckle involves the interfaces between the liquid, the membrane, and the substrate. In this case, the change of the interfacial energy should be written as $\Delta\gamma = \gamma_{ml} + \gamma_{sl} - \gamma_{ms}$, where $\gamma_{ml}, \gamma_{sl}$, and $\gamma_{ms}$ are the energy densities (per unit area) for the membrane-liquid interface, substrate-liquid interface, and membrane-substrate interface, respectively. We can further use Young–Dupré equations to derive

$$\Delta\gamma_{\text{liquid}} = \Gamma - \gamma_l(\cos\theta_s + \cos\theta_m), \tag{6}$$

where $\gamma_l$ is the surface tension of the liquid, and $\theta_s$ and $\theta_m$ are the liquid contact angles of the substrate and the membrane, respectively (Israelachvili, 2011). If given the surface tension of the confined liquid and its contact angle to the 2D material and the substrate, with $\Delta\gamma$ estimated by Eq. (4), one may extract the interface adhesion for the 2D material-substrate interface, a key interface parameter for 2D material-based devices (Koenig et al., 2011). It is worth mentioning that special attention should be given to the bending stiffness of 2D materials since the classical bending stiffness-Young's modulus relation for a plate breaks down when bending monolayer or multilayer 2D materials (Lu et al., 2009; Zhang et al., 2011; Wang et al., 2019).

The 1D analysis gives a characteristic length scale $\lambda^2/\delta \sim \sqrt{B/\Delta\gamma}$, which compares surface tension and/or adhesion with bending stiffness and has been referred to as the elasto-capillary length (Py et al., 2007; Schroll et al., 2013; Vella et al., 2009). Such scaling can explain our experimental observation of constant $\lambda^2/\delta$ in Fig. 2c although these radial buckles, unlike the 1D buckles, involve bending energy from two principal curvatures, i.e., both radial and circumferential. However, if the curvature of the crest line ($\kappa_r$) is much smaller than the hoop curvature of the buckle ($\kappa_\theta$) as illustrated in Fig. 3b, the bending energy of the radial buckle can reasonably reduce to the 1D estimate. Experimentally, we found that $\kappa_r$ decays over $r$ and the maximum $\kappa_r$ is found near the edge of the tent (~ 0.1 $\mu\text{m}^{-1}$ for monolayer $MoS_2$ tent) while the maximum $\kappa_\theta$ is at the buckle crest appearing to be a $r$-independent constant (~ 2 $\mu\text{m}^{-1}$). Indeed, $\kappa_r \ll \kappa_\theta$.

### 3.3. The formation mechanism of radial buckles

Having analyzed the hoop-direction profile characteristics of the 2D material radial buckles, we move on with the investigation of how these characteristic parameters vary with the radial position $r$. In Fig. 3c, we plot the measured $\lambda$, $\delta$, $\lambda^2/\delta$, $\delta^2/\lambda$ of the $MoS_2$ buckles shown in Fig. 2a vs. $r$. Here, our primary interest is in the size of the buckled region, which might be equivalent to the region in which there is a hoop compression (Vella et al., 2010). If we assume that the 2D material-substrate interface is frictionless, the 2D material inside the tent pulls the 2D material outside the tent inward, and hence the hoop stress is negative, leading to the buckle delamination of the atomically thin membrane, i.e. the 2D material. If we estimate the size of the buckled zone by the size of the compression zone, the analysis of $\Delta$~$r$ relation then becomes a classical problem of linear elasticity – the Lamé problem (Davidovitch et al., 2011; Sadd, 2009). We can, therefore, obtain the stress and displacement field of the planar, axisymmetric state and reach the conclusion that both stress and strain $\sim r^{-2}$ and $\Delta \sim r^{-1}$ if we apply a traction-free boundary condition at infinity (Davidovitch et al., 2011; Sadd, 2009). Combining with the characteristic length scale yields the following scaling predictions:

$$\Delta = \frac{\pi^4\delta^2}{4\lambda} \sim r^{-1},\ \frac{\lambda^2}{\delta} \sim \sqrt{\frac{B}{\Delta\gamma}} \sim r^0,\ \delta \sim r^{-2/3},\ \lambda \sim r^{-1/3}. \tag{7}$$

We plot these scaling relations in Fig. 3c and find reasonable agreement with experimental results. We thus suggest that the formation of the 2D material buckles around a tent is a result of interface sliding and their profiles are governed by the competition between the bending energy and the interface energies.

However, the frictionless assumption indicates that the entire substrate-supported part of the membrane undergoes the hoop compression and thus over-predicts the extent of the buckled region compared with that observed experimentally. Specifically, the best fittings in Fig. 3c (dashed lines) yield a much faster decay of $\Delta$ than $r^{-1}$ ($r^{-2.3\pm0.2}$ in fact), of $\delta$ than $r^{-2/3}$ ($r^{-1.5\pm0.1}$), as well as a slightly faster decay of $\lambda$ than $r^{-1/3}$ ($r^{-0.7\pm0.1}$). This motivates the following analysis accounting for above-overlooked factors such as interfacial shear traction, pretension, and the finite size of the nanopillar and the membrane, all of which may affect the size/extent of the zone subjected to hoop compression (we then call it the compression zone). Since these factors are possible to be controlled in experiments, knowing their effects may guide the rational design of 2D material tents with or without peripheral instabilities. Another important reason for the deviation between Lamé predictions and the observation in Fig. 3 is that a highly bendable sheet cannot sustain compressive stresses and instabilities occur and release the hoop compression (Box et al., 2019; Davidovitch and Vella, 2018). It is thus necessary to perform an analysis to consider that the negative stresses are relaxed in the membrane (frequently referred to as tension field theory or far-from threshold analysis) (Davidovitch et al., 2011; Vella, 2019). Note that such relaxation may not be complete for relatively thick 2D material membranes because of the stiff, adhesive substrate. We will demonstrate an example of this case in Section 8.

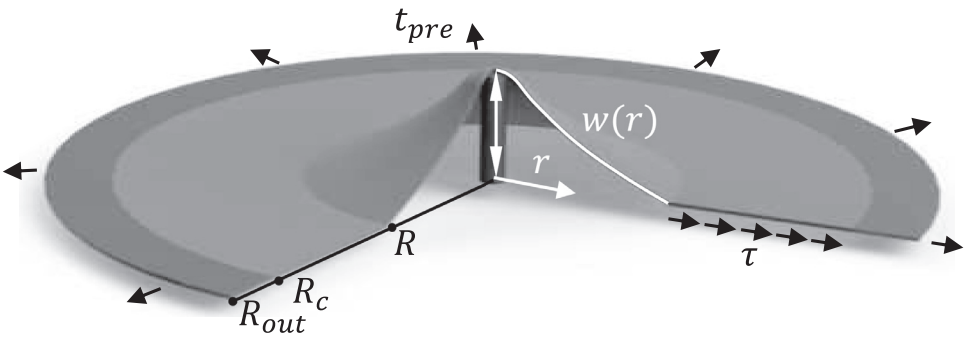


**Fig. 4.** Notations for the analysis of an axisymmetric tent where a finite zone in the substrate-supported regime ($R < r < R_c$) undergoes hoop compression caused by interface sliding. $R$ is the edge of the tent, $R_c$ is the edge of the compression/buckled zone, and $R_{out}$ is the outer radius of consideration. $\tau$ is the membrane-substrate interface shear traction and $t_{pre}$ is the pretension in the membrane.

Therefore, in the following sections, we first consider a limiting case in Section 4 assuming that the hoop compressive stress is maintained (instabilities are suppressed) such that we can adopt near-threshold (NT) modeling with the consideration of interfacial shear traction, pretension, and the finite size of pillar and membrane. Parametric studies based on NT modeling are performed in Section 5. For thin sheets, a more representative case arises from that the hoop compressive stress is fully relaxed. We describe this case through far-from-threshold (FFT) modeling in Section 6. The analysis of FFT modeling and its comparison with NT modeling are discussed in Section 7. The NT and FFT modeling would provide upper/lower limits for the tent system in general, and we will leverage them to interpret our experimental observations in Section 8.

## 4. Near-threshold modeling

### 4.1. General theory

We first present a theoretical framework for considering the finite interfacial shear traction between the 2D material and its substrate. We will show that other factors (i.e., pretension, and the finite size of the nanopillar and the membrane) come into play through boundary conditions. A theoretical idealization of an axisymmetric tent formed by 2D materials is shown in Fig. 4. Inside the tent ($r < R$), the vertical displacement $w(r)$ caused by a point load $F$ is related to the Airy stress function $\phi(r)$ by Föppl–von Kármán (FvK) equations (Mansfield, 2005; Vella and Davidovitch, 2017),

$$\nabla^2\left(B\nabla^2 w\right) - [\phi, w] - \frac{F}{2\pi}\frac{\delta(r)}{r} = 0 \tag{8}$$

and

$$\nabla^4\phi + \frac{1}{2}E_{2D}[w, w] = 0, \tag{9}$$

where $E_{2D}$ is the in-plane stiffness of the membrane, $\delta(r)$ is the Dirac delta function, the operators $[f, g] = (f_{,rr}g_{,r} + f_{,r}g_{,rr})/r$, $\nabla^2 f = f_{,rr} + f_{,r}/r$, $\nabla^4 = \nabla^2\nabla^2$, and $()_{,r}$ denotes differentiation with respect to $r$. The radial and circumferential stress resultants can take the form

$$N_{rr} = \phi_{,r}/r \text{ and } N_{\theta\theta} = \phi_{,rr}. \tag{10}$$

For the membrane outside the tent ($R < r < R_c$), we assume $w = 0$, i.e. no buckling and hence compressive stress not relaxed. $R_c$ is the outer radius of the compression zone. Considering the thinness of 2D materials, we can treat the interface shear traction, $\tau$, as a body force and assume that it is derivable from an in-plane potential function $v$ such that (Sadd, 2009)

$$v_{,r} + \tau = 0. \tag{11}$$

This assumption is not very restrictive because many models about interfacial interactions between the 2D material and its substrate followed this approach (Zhang and Tadmor, 2018). The equilibrium can be automatically satisfied by taking stress resultants as

$$N_{rr} = \phi_{,r}/r + v \text{ and } N_{\theta\theta} = \phi_{,rr} + v. \tag{12}$$

In the NT analysis, the strain compatibility holds and provides the governing equation

$$\nabla^4\phi + (1-\nu)\nabla^2 v = 0. \tag{13}$$

### 4.2. Non-dimensionalization

Eqs. (8)–(13) complete the governing equations for the tent problem accounting for finite interface shear, which are to be solved along with boundary conditions. Before proceeding, we note that the first term in Eq. (8), representing bending, can be neglected due to the thinness of 2D materials. The tent radius $R$ and the membrane stiffness $E_{2D}$ are experimentally accessible, and sometimes (e.g. in nanoindentation tests) the radius is prescribed by a hole patterned on the substrate. We then use these two quantities to non-dimensionlize the variables as follows

$$\rho = \frac{r}{R},\ \rho_c = \frac{R_c}{R},\ W = \frac{w}{R},\ \bar{F} = \frac{F}{E_{2D}R},\ \Phi = \frac{\phi}{E_{2D}R^2},\ \mathrm{T} = \frac{\tau R}{E_{2D}},\ V = \frac{v}{E_{2D}}. \tag{14}$$

Now, inside the tent ($\rho \le 1$), we integrate Eqs. (8) and (9) once and find that (Chopin et al., 2008)

$$\Phi' W' + \frac{\bar{F}}{2\pi} = 0 \tag{15}$$

and

$$\rho \frac{\mathrm{d}}{\mathrm{d}\rho}\left[\frac{1}{\rho}\frac{\mathrm{d}}{\mathrm{d}\rho}\left(\rho\Phi'\right)\right] + \frac{1}{2}W'^2 = 0, \tag{16}$$

where $()'$ denotes differentiation with respect to $\rho$. Outside the tent ($1 \le \rho \le \rho_c$), Eqs. (11) and (13) become

$$V' + T = 0 \tag{17}$$

and

$$\frac{\mathrm{d}}{\mathrm{d}\rho}\left[\frac{1}{\rho}\frac{\mathrm{d}}{\mathrm{d}\rho}\left(\rho\Phi'\right)\right] + (1-\nu)V' = 0. \tag{18}$$

The four boundary value problems, i.e. $\Phi'(\rho)$ and $W(\rho)$ when $\rho \le 1$, and $\Phi'(\rho)$ and $V(\rho)$ when $\rho \ge 1$, can be solved according to boundary conditions. In this work, we present closed-form analytical solutions to them, by which several useful composite parameters emerge naturally and relate to experiments directly.

### 4.3. Analytical results: outside the tent

There has been a surge of interest in the sliding between 2D materials and their substrates in recent years (Xu and Zheng, 2018). Micro-scale Raman characterizations indicated nonlinear shear responses of the 2D material-substrate interface (Dai et al., 2016; Guo and Zhu, 2015; Jiang et al., 2013; Wang et al., 2016; Wang et al., 2017b). Moreover, many subtle features of the interface shear/friction appeared when measurement resolutions downsized to the atomic level (Kitt et al., 2013; Wang et al., 2017c). For example, the frictional resistance is found to be particularly sensitive to chemical bonding, substrate roughness, and the local lattice state of the interface. So-call superlubricity (a nearly frictionless state) can be achieved between incommensurately stacked 2D materials (Liu et al., 2012). Here, we take the first-order approximation and assume a constant interface shear traction within the sliding zone (i.e. the compression zone), like the perfect plasticity behaviors (Gong et al., 2010; Kitt et al., 2013; Wang et al., 2017a). With this simplification, Eq. (17) can be integrated once such that

$$V = -T\rho + A. \tag{19}$$

Eq. (18) can then be solved directly

$$\Phi'(\rho) = B\rho + \frac{C}{\rho} + \frac{1-\nu}{3}T\rho^2. \tag{20}$$

At the outer edge of the circumferentially compressed zone ($\rho = \rho_c$), both radial and circumferential stress resultants decay to zero, i.e. $\Phi'(\rho_c)/\rho_c + V = \Phi''(\rho_c) + V = 0$, leading to

$$A + B = \frac{1+\nu}{2}T\rho_c \text{ and } C = \frac{1-\nu}{6}T\rho_c^3. \tag{21}$$

### 4.4. Analytical results: inside the tent

Nonlinear FvK equations for thin membranes are difficult to solve, but analytical progress has been recently made for axisymmetric cases (Jin et al., 2017; Vella and Davidovitch, 2017; Vella and Davidovitch, 2018). Here, we adopted the strategy proposed by Chopin et al. (2008) and Vella and Davidovitch (2017). Using Eq. (15) can eliminate $W'$ in Eq. (16),

$$\rho \frac{\mathrm{d}}{\mathrm{d}\rho}\left[\frac{1}{\rho}\frac{\mathrm{d}}{\mathrm{d}\rho}\left(\rho\Phi'\right)\right] + \frac{1}{2}\left(\frac{\bar{F}}{2\pi\Phi'}\right)^2 = 0. \tag{22}$$

It is convenient to introduce (Bhatia and Nachbar, 1968)

$$\psi(\eta) = \rho\Phi'(\rho),\ \ \eta = \rho^2, \tag{23}$$

such that Eq. (22) can be simplified as

$$\frac{\mathrm{d}^2\psi}{\mathrm{d}\eta^2} = -\frac{\bar{F}^2}{32\pi^2\psi^2}. \tag{24}$$

We integrate once to obtain

$$\frac{\mathrm{d}\psi}{\mathrm{d}\eta} = \frac{\bar{F}}{4\pi}\sqrt{(\alpha\psi+1)/\psi}, \tag{25}$$

where $\alpha$ is a negative constant to be determined based on boundary conditions. Using $\tilde{\psi} = -\alpha\psi$, Eq. (25) becomes

$$\frac{\mathrm{d}\tilde{\psi}}{\mathrm{d}\eta} = \frac{\bar{F}\sqrt{(-\alpha)^3}}{4\pi}\sqrt{\left(1-\tilde{\psi}\right)/\tilde{\psi}}. \tag{26}$$

Further integrating analytically (Chopin et al., 2008), we have

$$\frac{\bar{F}\sqrt{(-\alpha)^3}}{4\pi}\eta = -\sqrt{\tilde{\psi}\left(1-\tilde{\psi}\right)} + \tan^{-1}\sqrt{\tilde{\psi}/\left(1-\tilde{\psi}\right)}, \tag{27}$$

where we used the zero radial displacement condition at the center of the tent, i.e. $\lim_{\rho\to 0}\rho[\phi''(\rho)-\nu\phi'(\rho)] = 0$ or essentially

$$\tilde{\psi}(0) = 0. \tag{28}$$

At the edge of the tent ($\eta = 1$), a useful parameter $\tilde{\psi}_1 = \tilde{\psi}(1)$ can be defined that satisfies

$$\frac{\bar{F}\sqrt{(-\alpha)^3}}{4\pi} = -\sqrt{\tilde{\psi}_1\left(1-\tilde{\psi}_1\right)} + \tan^{-1}\sqrt{\tilde{\psi}_1/\left(1-\tilde{\psi}_1\right)}. \tag{29}$$

Invoking the continuity condition of radial stress and displacement, we have

$$\Phi'\left(1^-\right) = \Phi'\left(1^+\right) + V\left(1^+\right) \text{ and } \Phi''\left(1^-\right) - \nu\Phi'\left(1^-\right) = \Phi''\left(1^+\right) - \nu\Phi'\left(1^+\right) + (1-\nu)V\left(1^+\right), \tag{30}$$

which further lead to

$$\tilde{\psi}_1 = -\alpha T\left(\frac{1+\nu}{2}\rho_c + \frac{1-\nu}{6}\rho_c^3 - \frac{2+\nu}{3}\right) \tag{31}$$

and

$$\frac{\mathrm{d}\tilde{\psi}}{\mathrm{d}\eta}|_{\eta=1} = -\alpha T\frac{1+\nu}{2}(\rho_c - 1). \tag{32}$$

Ostensibly, the boundary value problem in Eq. (24) is a 2nd order system with three boundary conditions, i.e., Eqs. (28), (31), and (32). However, the size of the compression zone, $\rho_c$, is unknown. In fact, Eq. (32) can be used to give an equation for the integration constant $\alpha$ in Eq. (26)

$$-\alpha T\frac{1+\nu}{2}(\rho_c - 1) = \frac{\bar{F}(-\alpha)^{3/2}}{4\pi}\sqrt{\frac{1-\tilde{\psi}_1}{\tilde{\psi}_1}}. \tag{33}$$

Further, combining Eqs. (29) and (33) can eliminate $\bar{F}$ and relate the $\alpha$ to $\tilde{\psi}_1$, $T$, and $\rho_c$ by

$$\alpha = \frac{2\left[1-\tilde{\psi}_1 - \sqrt{\left(1-\tilde{\psi}_1\right)/\tilde{\psi}_1}\tan^{-1}\sqrt{\tilde{\psi}_1/\left(1-\tilde{\psi}_1\right)}\right]}{(1+\nu)T(\rho_c-1)}. \tag{34}$$

We then use Eq. (34) to eliminate the constant $\alpha$ in Eq. (31), and finally, find $\tilde{\psi}_1$ as a function of $\rho_c$

$$\frac{3(1+\nu)(\rho_c-1)}{\left[3(1+\nu)\rho_c + (1-\nu)\rho_c^3 - 2(2+\nu)\right]} = 1 - \tilde{\psi}_1^{-1} + \sqrt{\left(1-\tilde{\psi}_1\right)/\tilde{\psi}_1^3}\tan^{-1}\sqrt{\tilde{\psi}_1/\left(1-\tilde{\psi}_1\right)}. \tag{35}$$

It is found that $\tilde{\psi}_1 \to 1$ represents the ultra-lubricated membrane-substrate interface as the size of the compression zone $\rho_c$ goes infinity. In general, for a given size of the compression zone $\rho_c$, we can figure out the required parameters $\tilde{\psi}_1$ by Eq. (35), $\alpha$ by Eq. (34), and then the point force $\bar{F}$ by Eq. (33) in terms of the interfacial shear traction $T$.

### 4.5. A composite parameter

We aim to relate to the size of the compression zone $\rho_c$ to the center height of the tent $W_0 = W(0)$ because the latter one is experimentally accessible. Note that from Eq. (15),

$$W_0 = \int_0^1 \frac{\bar{F} d\rho}{2\pi \Phi'} = \frac{-\bar{F}\alpha}{4\pi} \int_0^{\tilde{\psi}_1} \frac{d\tilde{\psi}}{\tilde{\psi}\tilde{\psi}'}. \tag{36}$$

Combining Eq. (36) with Eq. (26) can analytically obtain

$$W_0 = \frac{2}{\sqrt{-\alpha}} \tan^{-1} \sqrt{\tilde{\psi}_1 / \left(1 - \tilde{\psi}_1\right)}. \tag{37}$$

Eqs. (34), (35), and (37) complete the analytical solutions to the problem where a circular membrane is poked with a height of $W_0$ and is supported by an interface with a constant shear traction $T$. Particularly, Eqs. (34) and (37) can cancel the constant $\alpha$ out and hence the size of the compressive/buckling zone $\rho_c$ depends on a single composite parameter $T/W_0^2$. This suggests that reducing the interfacial shear resistance and increasing the tent height can extend the compression zone outside the tent.

## 5. Parametric studies based on near-threshold modeling

Based on NT modeling, we now present how the size of the compression zone changes with the height of the tent and other parameters of the system including the shear traction of the 2D material-substrate interface, pretension in the 2D material, size of the 2D material, and the pillar radius.

### 5.1. Interfacial shear traction

We start with the distribution of the hoop compressive displacement in the substrate-supported region ($\rho \geq 1$) by considering the shortened perimeter of a material circle. Hooke's law can relate the hoop strain to stress resultants by

$$\epsilon_{\theta\theta} = \frac{N_{\theta\theta} - \nu N_{rr}}{E_{2D}}. \tag{38}$$

The stress resultants can be readily calculated through Eqs. (12) and (19)–(21). We normalize the hoop compression by the tent radius such that

$$\bar{\Delta} = -\frac{2\pi r \epsilon_{\theta\theta}}{R} = \frac{\pi\left(1-\nu^2\right)}{3} T\rho \left(-3\rho_c + \frac{\rho_c^3}{\rho^2} + 2\rho\right). \tag{39}$$

In Fig. 5a, we plot $\bar{\Delta}$ as a function of $\rho$ for tents subject to different center heights and various interfacial tractions. Evidently, when $T \to 0$, the limit of $\bar{\Delta}(\rho) \sim \rho^{-1}$ can be observed, which is consistent with what was predicted under the assumption of the frictionless interface in Section 3.3. The maximum compressive displacement is thus located at the edge of the tent, i.e. $\bar{\Delta}_1 = \bar{\Delta}(1)$. However, with finite interfacial shear traction, the compression zone outside the tent is confined within a finite region ($1 \leq \rho \leq \rho_c$). As a result, the hoop compressive displacement decays faster than $\rho^{-1}$ when approaching $\rho_c$, especially for tents with small center heights. The detailed size of the compression zone versus center height for various interfacial tractions is further plotted in Fig. 5b. As expected, large center deflection and weak shear traction at the membrane-substrate interface can facilitate the propagation of the compression zone in the supported region. Notably, both $\bar{\Delta}_1/W_0^2$ and $\rho_c$ depend on a composite parameter $T/W_0^2$ monotonically and the corresponding master curves are shown in Fig. 5c and d. We may point out that this composite parameter compares the shear traction at the interface with the stretching forces in the membrane since the latter one scales as $W_0^2$ inside the tent.

### 5.2. Pretension

We consider the pretension ($T_{pre} = t_{pre}/E_{2D}$, Fig. 4) in 2D materials that may be introduced when transferring them to target substrates (Brennan et al., 2015). For simplicity, we focus on a limiting case – frictionless interface – such that the general solution for the Airy stress function outside the tent (also known to Lamé) takes a simple form

$$\Phi' = a\rho + b/\rho. \tag{40}$$

In addition, we expect $a = T_{pre}$ since the stress resultants approach the applied pretension as $\rho \to \infty$. The constant $b$ can be determined analytically in terms of the applied pretension $T_{pre}$ and the center height of the tent $W_0$ based on the continuity conditions at the edge of the tent Appendix A). With Eqs. (38)–(40), we can derive circumferential compressive displacement

$$\bar{\Delta} = 2\pi(1+\nu)b/\rho - 2\pi(1-\nu)T_{pre}\rho. \tag{41}$$

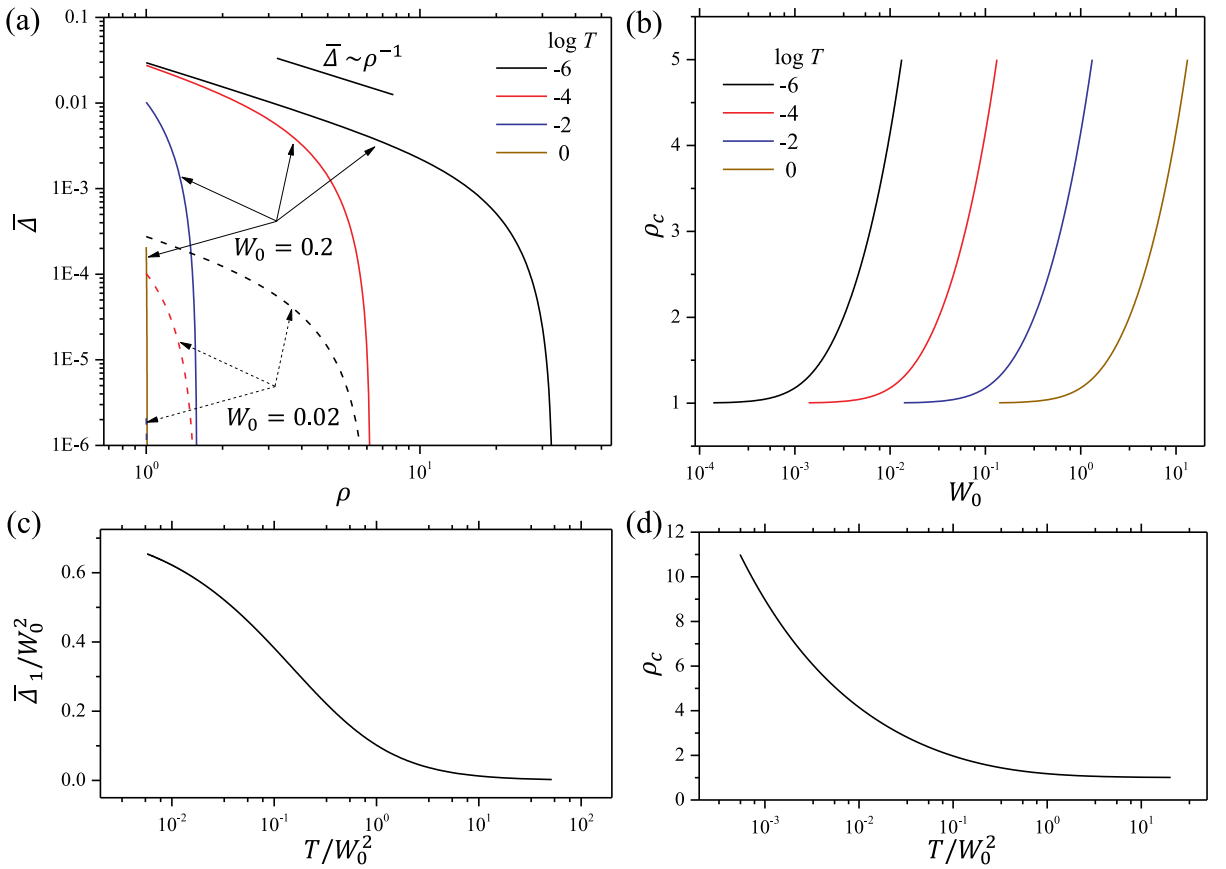


**Fig. 5.** (a) Hoop compressive displacement along the radial direction for various interfacial shear tractions. Solid curves denote tents with a center height $W_0 = 0.2$ while dashed curves denote $W_0 = 0.02$. (b) The size of the compression zone versus the center height of the tent for various interfacial shear tractions. (c) The dependency on $T/W_0^2$ of the hoop compressive displacement at the edge of the tent. (d) The dependency on $T/W_0^2$ of the size of the compression zone. All quantities are normalized quantities in this figure.

Fig. 6a shows the $\bar{\Delta}$ as a function of $\rho$ for tents subject to different center heights and various values of pretension. Analogous to the effect of $T$ in Fig. 5a, the distribution of compressive displacement approaches $\bar{\Delta} \sim \rho^{-1}$ as $T_{pre} \to 0$. Also, the finite pretension makes the decay of $\bar{\Delta}$ faster than $\rho^{-1}$, especially for tents with small center deflections since the size of the compression zone outside the tent becomes finite. These results are similar to the finite wrinkling zone of a thin polymeric film floating on the water surface while undergoing a point force at the center and surface tension at the edge of the film (Vella et al., 2015).

We find that when pretension exists, a critical center deflection is required for the onset of the compression zone outside the tent. For example, in the cases of $T_{pre} \geq 10^{-3}$ and $W_0 = 0.03$ in Fig. 6a, the thin sheet is subject to tension everywhere across its entire area and hence, circumferential compression is prohibited. This phenomenon can be further elucidated by $\rho_c \sim W_0$ curves in Fig. 6b where the outer radius of the compression zone is identified by

$$\bar{\Delta}(\rho_c) = 0. \tag{42}$$

Clearly, the critical center deflection ensuring $\rho_c > 1$ increases with increasing pretension in the membrane. Interestingly, the normalized maximum compressive displacement ($\bar{\Delta}_1/W_0^2$) and the size of the compression zone ($\rho_c$) depend on a composite parameter $T_{pre}/W_0^2$ as shown in Fig. 6c and d (Appendix A). As the center deflection of the tent causes a strain scaling as $(w(0)/R)^2$ or $W_0^2$, and associated stress scaling as $E_{2D}W_0^2$, the composite parameter, $T_{pre}/W_0^2$, thus compares the pre-stress with the stress associated with the out-of-plane deformation of the tent. Notably, buckling instabilities are likely to occur only when $T_{pre}/W_0^2 \lesssim 0.12$. When the interfacial shear traction is considered, we expect two governing parameters: $T_{pre}/W_0^2$ and $T/W_0^2$.

### 5.3. Finite size of 2D materials

We now turn to the case that the compression zone engulfs the entire membrane since the size of the 2D materials ($\rho_{out} = R_{out}/R$, Fig. 4) is typically limited in experiments. Before the outer edge of the compression zone approaches the

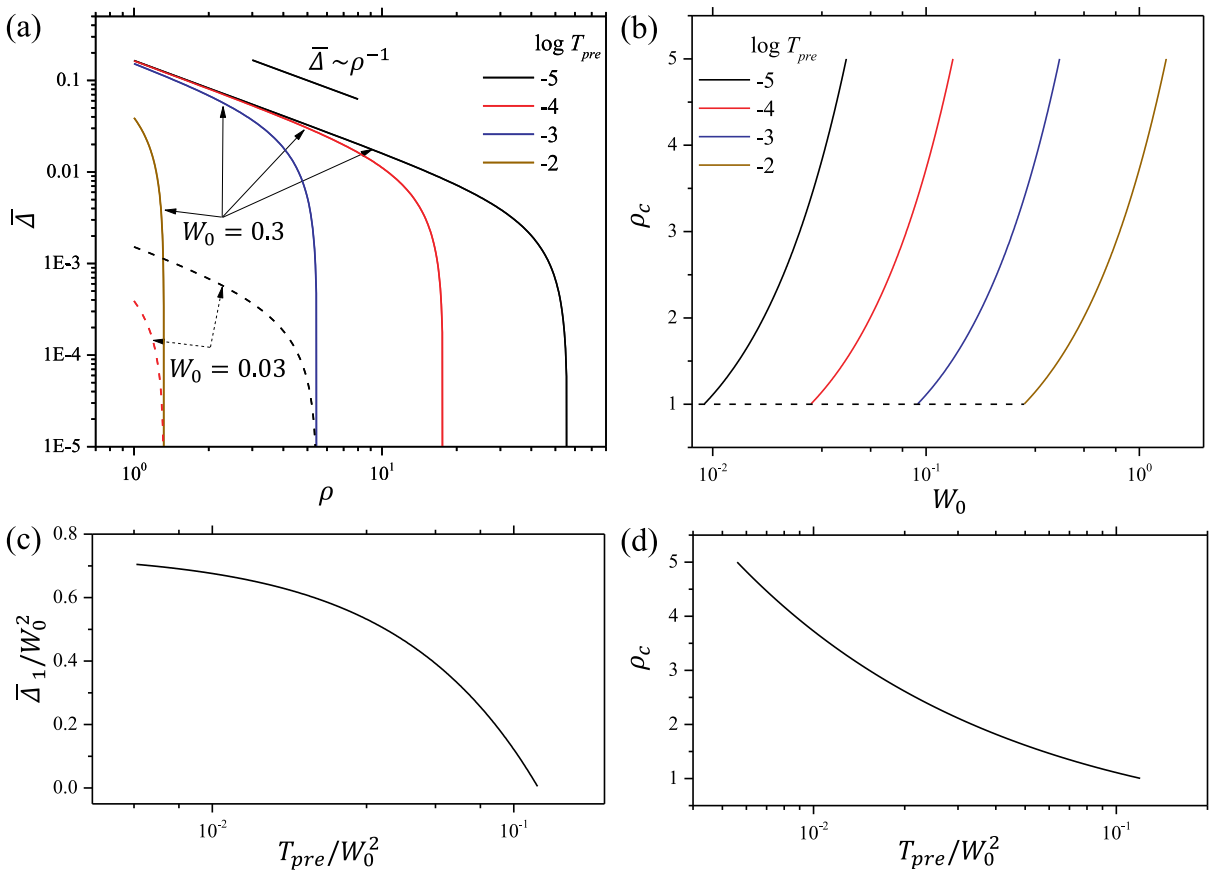


**Fig. 6.** (a) Hoop compressive displacement along the radial direction for different values of pretension. Solid curves denote tents with a center height $W_0 = 0.3$ while dashed curves denote $W_0 = 0.03$. Note that for the cases of $T_{pre} = 10^{-3}$ and $10^{-2}$, the tent of $W_0 = 0.03$ shows hoop tension across the entire membrane indeed. (b) The size of the compression zone versus the center height of the tent for different values of pretension. The dashed line shows that a critical center deflection is required for the onset of a compression zone outside the tent due to the existence of pretension. (c) The dependency on $T_{pre}/W_0^2$ of the compressive displacement at the edge of the tent. (d) The dependency on $T_{pre}/W_0^2$ of the size of the compression zone. All quantities are normalized quantities in this figure.

edge of the 2D material flake ($\rho_c \leq \rho_{out}$), our analysis in Section 5.1. should still hold. However, when $\rho_c \equiv \rho_{out}$, we neglect the pretension for simplicity such that the edge of the membrane becomes traction-free, i.e., $N_{rr}(\rho_{out}) = 0$, or

$$\frac{\Phi'(\rho_{out})}{\rho_{out}} + V = 0. \tag{43}$$

We then write circumferential compressive displacement regarding the interfacial shear traction and the size of the 2D material

$$\overline{\Delta} = 2\pi T \rho \left[ \frac{C}{T} \left( \frac{1-\nu}{\rho_{out}^2} + \frac{1+\nu}{\rho^2} \right) - \frac{1-\nu^2}{3} \left( \frac{2+\nu}{1+\nu} \rho_{out} - \rho \right) \right], \tag{44}$$

where the constant $C$ can be determined by the abundant continuity conditions at the edge of the tent (Appendix B).

Fig. 7a shows the evolution of $\bar{\Delta}$ with increasing tent height where solid curves represent membranes with $\rho_{out}$ of 3 and dashed curves represent sufficiently large membranes ($\rho_{out} > \rho_c$). After $\rho_c \to 3$, differences between the two types of tents appear regarding the displacement fields. Specifically, further increasing the center height of the tent, dashed curves approach $\bar{\Delta} \sim \rho^{-1}$ from below (the same as the observations in Fig. 5), while solid curves show larger compressive displacement and even overshoot the $\bar{\Delta} \sim \rho^{-1}$ limit near the outer edge of the thin membrane. In addition, we found that $C/T$ is a function of the parameters $T/W_0^2$ and $\rho_{out}$ (Appendix B), as is the normalized compressive displacement at the edge of the tent $\bar{\Delta}_1/W_0^2$ as shown in Fig. 7. When the pretension is considered, we expect three governing parameters in this system: $T_{pre}/W_0^2$, $T/W_0^2$ and $\rho_{out}$.

### 5.4. Finite pillar radius

Up to now, we have assumed a point force acting at the tent center. However, in many experimental setups, the radius of the pillar ($\rho_{in} = R_{in}/R$) is finite, which may have a nontrivial effect on the size of the compression zone. When accounting

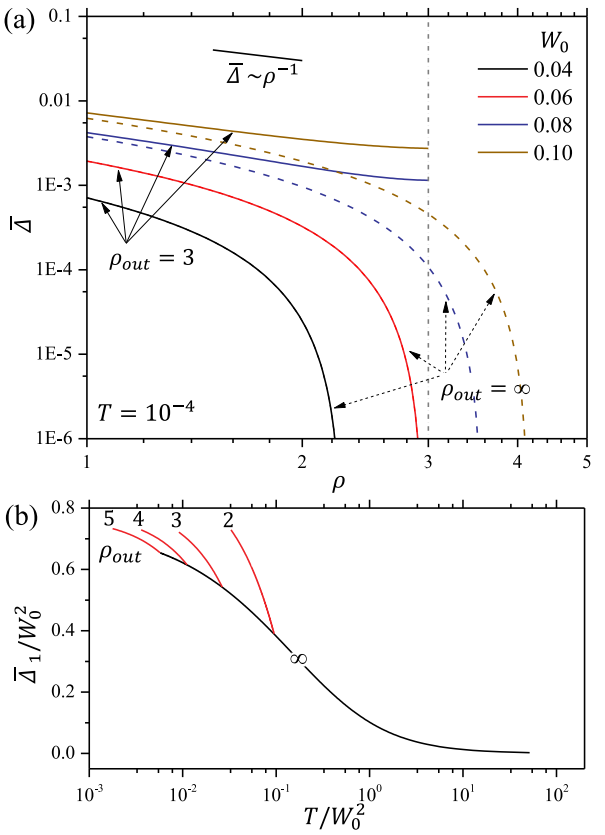


**Fig. 7.** (a) Hoop compressive displacement along the radial direction for tents with various center heights. Solid curves denote tents with an outer radius $\rho_{out} = 3$ while dashed curves denote the case where the membrane size is sufficiently large. Note that when the center height is small (i.e. $W_0 = 0.04$ and 0.06), the solid and dashed curves overlap because $\rho_c \leq \rho_{out}$. (b) The dependency on $T/W_0^2$ of the normalized compressive displacement at the edge of the tent.

for the finite radius of the circular plateau at the tip of the pillar, the differential equations inside the tent, i.e., Eqs. (15) and (16), are still applicable, while the integrating domain to derive them becomes $[\rho_{in}, 1]$. We may consider the following "boundary" values at the edge of the pillar and tent,

$$W(\rho_{in}) = W_0,\ \tilde{\psi}\left(\rho_{in}^2\right) = \tilde{\psi}_{in}, \tilde{\psi}(1) = \tilde{\psi}_1. \tag{45}$$

$\tilde{\psi}_1$ is constrained by the continuity conditions and then relates to the size of the compression zone by Eq. (30). In addition, we assume that the radial displacement is fixed at the edge of the pillar for simplicity that requires

$$\frac{\mathrm{d}\tilde{\psi}}{\mathrm{d}\eta}|_{\eta=\rho_{in}^2} = \frac{1+\nu}{2}\frac{\tilde{\psi}_{in}}{\rho_{in}^2}. \tag{46}$$

We still pursue exact analytical solutions using the same technique as outlined in Section 4 (effects of the finite size of the 2D material and pretension are neglected, see details in Appendix C). This allows us to eliminate intermediate parameters and find out governing ones: the radius of the pillar and the combined parameter $T/W_0^2$. In Fig. 8, we show the dependency of the normalized compressive displacement at the edge of the tent $\bar{\Delta}_1/W_0^2$ and the size of the compression zone $\rho_c$ on $\rho_{in}$ and $T/W_0^2$. As $\rho_{in} \to 0$, we verify that these results recover those obtained by assuming a point force in Fig. 5. Furthermore, we find that the hoop compression at the edge of the tent increases significantly as the pillar radius increases from 0.001 to 0.25, (Fig. 8a) while the size of the compression zone increases slightly (Fig. 8b). When the finite size of the 2D material and pretension are considered, we expect four governing parameters: $T_{pre}/W_0^2$, $T/W_0^2$, $\rho_{in}$, and $\rho_{out}$.

## 6. Far-from-threshold modeling

Based on the NT analysis, we have derived four controlling parameters exactly: $T/W_0^2$, $T_{pre}/W_0^2$, $\rho_{out}$, and $\rho_{in}$. However, such analysis may approximate well only when the sheet is very thick and the substrate can largely constrain the formation of the buckling (the ~15-layer graphene sample shown in Fig. 15 would be an example). FFT analysis comes naturally from that buckle instabilities occur and relax the hoop compressive stress such that $N_{\theta\theta} \approx 0$ or $|N_{\theta\theta}| \ll N_{rr}$

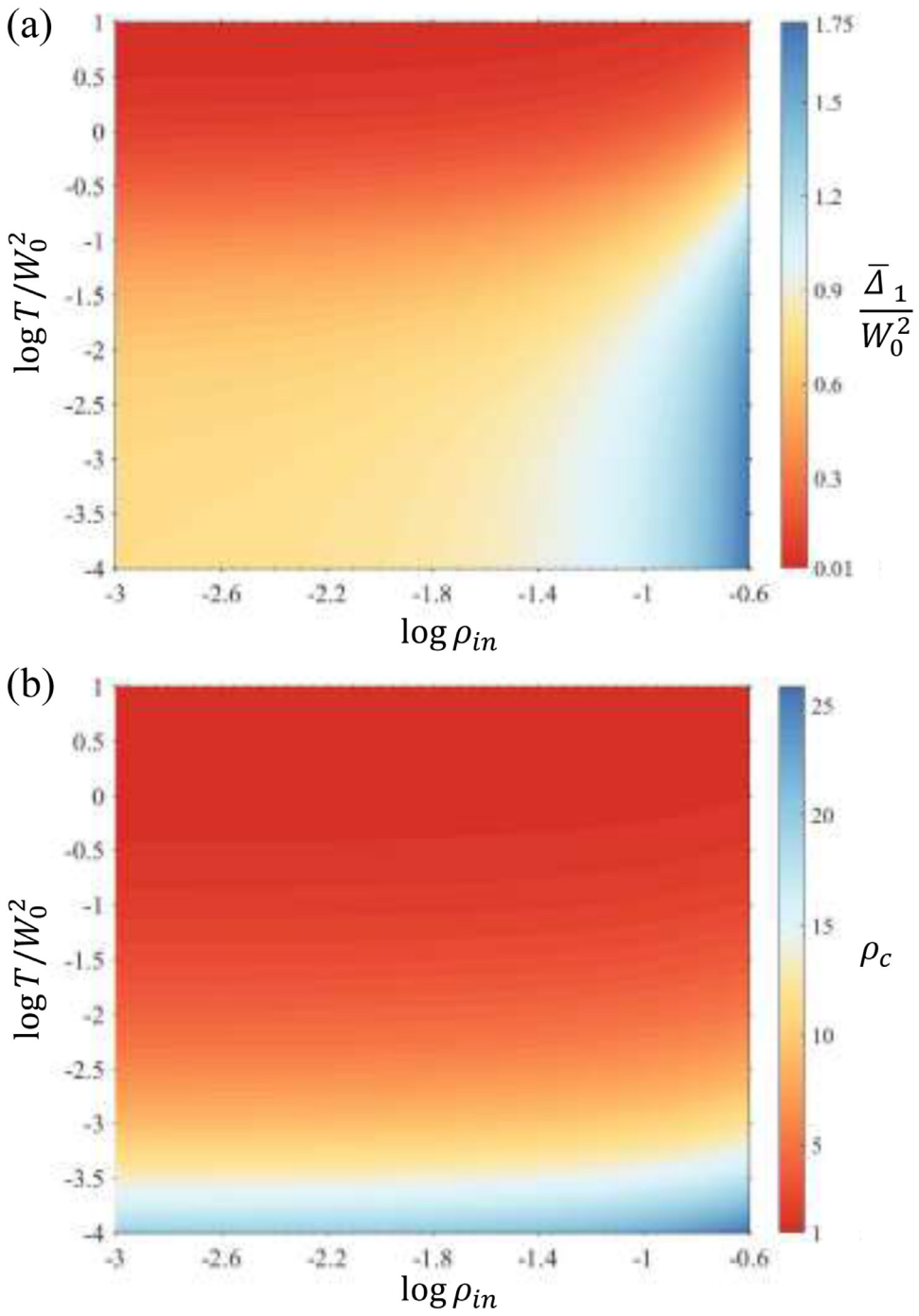


**Fig. 8.** Contour plots for the normalized compressive displacement at the edge of the tent $\bar{\Delta}_1/W_0^2$ (a) and the size of the compression zone $\rho_c$ (b) as a function of two governing parameters: $\rho_{in}$ and $T/W_0^2$.

(Davidovitch et al., 2011; Vella and Davidovitch, 2018). This scenario would be particularly true for a highly bendable sheet that is wrinkled in the suspended region and buckled in the substrate-supported region, for example, the monolayer $MoS_2$ sample shown in Fig. 2a right panel and Fig. 14. As a result, a number of regions should be considered in general, including a central suspended and unwrinkled region [0, $\rho_w$], a suspended and wrinkled region [$\rho_w$, 1], a supported and buckled region outside the tent [1, $\rho_b$], and then an outmost unbuckled region [$\rho_b$, $\rho_c$]. In this case, the size of buckled zone can be estimated by the size of the zero-$N_{\theta\theta}$ region (denoted by $\rho_b$). Note that the last region needs more thoughts when the pretension applies or when the buckled zone propagates and engulfs the finite membrane. For simplicity, we neglect the

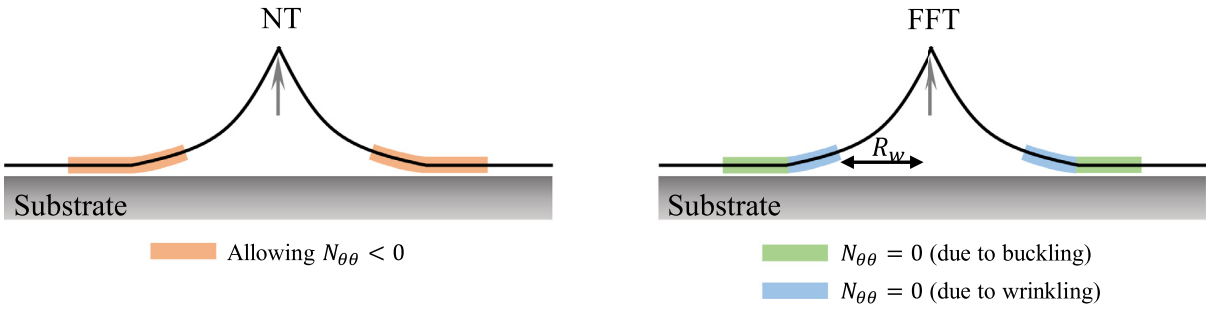


**Fig. 9.** Schematic illustration of the difference between near-threshold (NT) and far-from-threshold (FFT) modeling of a thin sheet tent.

finite size effect of the sheet and the pretension (due to a number of uncertainties as discussed later in Section 8.2.) for this FFT analysis and focus on the main physics associated with the interfacial shear traction.

We define $\rho = \rho_w$ (i.e. $r = \rho_w R$) as the boundary between the unwrinkled and wrinkled region in the suspended region of a tent Fig. 9). When $0 \le \rho \le \rho_w$, the regular FvK equations, i.e. Eqs. (15) and ((16), and their analytical solutions, still apply. Particularly, at $\rho = \rho_w$, we can define a useful parameter $\tilde{\psi}_w = \tilde{\psi}(\rho_w^2)$ that satisfies

$$\frac{\bar{F}\sqrt{(-\alpha)^3}}{4\pi}\rho_w^2 = -\sqrt{\tilde{\psi}_w\left(1-\tilde{\psi}_w\right)} + \tan^{-1}\sqrt{\tilde{\psi}_w/\left(1-\tilde{\psi}_w\right)}. \tag{47}$$

At this boundary, we also let the hoop stress be zero (Vella and Davidovitch, 2018) and, according to Eq. (26), obtain

$$\frac{\bar{F}\sqrt{(-\alpha)^3}}{2\pi}\rho_w^2 = \sqrt{\frac{\tilde{\psi}_w^3}{\left(1-\tilde{\psi}_w\right)}}. \tag{48}$$

Interestingly, combining Eqs. (47) and (48) can eliminate $\bar{F}$, $\alpha$, and $\rho_w$ simultaneously, such that $\tilde{\psi}_w$ must satisfy the transcendental equation

$$\sqrt{\tilde{\psi}_w^3/\left(1-\tilde{\psi}_w\right)} + 2\sqrt{\tilde{\psi}_w\left(1-\tilde{\psi}_w\right)} = 2\tan^{-1}\sqrt{\tilde{\psi}_w/\left(1-\tilde{\psi}_w\right)}, \tag{49}$$

whose nontrivial solution is $\tilde{\psi}_w \cong 0.6965$. However, $\rho_w$ is not known *a priori*, which prevents the solution to $\bar{F}\sqrt{(-\alpha)^3}$.

To deal with this unknown, we move on to the wrinkled region, $\rho_w \le \rho \le 1$, within which the second FvK equation concerning the compatibility is replaced by $N_{\theta\theta} = 0$. This leads to a constant $\Phi'$, and a linear out-of-plane profile of the tent according to the first FvK equation (within which $\bar{F} = 0$),

$$\Phi' = -\frac{\tilde{\psi}_w}{\alpha\rho_w} \text{ and } W = C_w(1-\rho), \tag{50}$$

where we used the continuity of radial stress at $\rho = \rho_w$ and the boundary condition $W(1) = 0$. To ensure the continuity of in-plane displacement ($u = R\tilde{u}$), we recall the kinematics within the wrinkled region to show that

$$\epsilon_{\rho\rho} = \frac{d\tilde{u}}{d\rho} + \frac{1}{2}\left(\frac{dW}{d\rho}\right)^2 \text{ or } -\frac{\tilde{\psi}_w}{\alpha\rho_w\rho} = \frac{d\tilde{u}}{d\rho} + \frac{1}{2}C_w^2. \tag{51}$$

Integrating Eq. (51) once, we have

$$\tilde{u}(\rho_w) - \tilde{u}(1) = -\frac{\tilde{\psi}_w}{\alpha\rho_w}\ln\rho_w + \frac{1}{2}C_w^2(1-\rho_w). \tag{52}$$

This means the in-plane displacement difference across the wrinkled region is enlarged by the in-plane stretch of the sheet (since $\rho_w \le 1$ and $\alpha < 0$) while reduced by the out-of-plane rotation of the sheet. We can detail $\tilde{u}(\rho_w)$ by Hooke's law and stress states in the unwrinkled region at $\rho = \rho_w$,

$$\tilde{u}(\rho_w) = \frac{\rho_w(N_{\theta\theta} - \nu N_{rr})}{E_{2D}} = \nu\frac{\tilde{\psi}_w}{\alpha\rho_w}. \tag{53}$$

To detail $\tilde{u}(1)$, we consider the stress field in the compression-free, supported region ($1 \le \rho \le \rho_b$) where Eq. (18) is modified by the release of the hoop stress due to buckling. We rewrite the in-plane force balance equation that reads

$$\frac{d}{dr}(rN_{rr}) + \tau r = 0. \tag{54}$$

We can find the exact solution to Eq. (54) when the pretension is absent (see Appendix D),

$$\frac{N_{rr}}{E_{2D}} = \frac{T}{2}\left(\rho_b^2\rho^{-1} - \rho\right) + C_N T\rho^{-1}, \tag{55}$$

where $C_N = -\frac{2+\nu}{3}\rho_b^2 - \frac{\nu-1}{6}\rho_c^3\rho_b^{-1} + \frac{1+\nu}{2}\rho_c\rho_b$ and $\rho_b = \frac{1-\nu+\sqrt{9+6\nu-15\nu^2}}{4+8\nu}\rho_c$. The associated displacement at the edge of the tent,

$$\tilde{u}(1) = \int_{\rho_c}^{1} \frac{N_{rr}}{E_{2D}} d\rho = \frac{T}{4}\left(-2\rho_b^2 \ln\rho_b + \rho_b^2 - 1\right) - C_N T \ln\rho_b + C_\nu T \rho_b \rho_c, \tag{56}$$

where $C_\nu = \nu(1+\nu)[-3(1+3\nu) + \sqrt{3(1-\nu)(3+5\nu)}]/(4+8\nu)$. The continuity of radial stress at $\rho = 1$ can then give rise to

$$\alpha\rho_w T\left(\rho_b^2 - 1\right) + 2\tilde{\psi}_w + 2\alpha C_N T\rho_w = 0 \tag{57}$$

and the continuity of the in-plane displacement, together with Eqs. (52) and (53), leads to

$$\frac{\tilde{\psi}_w}{\rho_w}\ln\rho_w - \frac{\alpha C_w^2}{2}(1-\rho_w) + \frac{\nu\tilde{\psi}_w}{\rho_w} - \frac{\alpha T}{4}\left(-2\rho_b^2\ln\rho_b + \rho_b^2 - 1\right) + \alpha C_N T\ln\rho_b - \alpha C_\nu T\rho_b\rho_c = 0. \tag{58}$$

Along the line of NT modeling in Section 4, we relate the parameter of interest (i.e. $\rho_c$ and $\rho_w$) to the center height of the tent,

$$W_0 = W(\rho_w) + \int_{\rho_w}^{0} \frac{-\bar{F}d\rho}{2\pi\Phi'} = C_w(1-\rho_w) + \frac{2}{\sqrt{-\alpha}}\tan^{-1}\sqrt{\tilde{\psi}_w/\left(1-\tilde{\psi}_w\right)}. \tag{59}$$

Finally, the continuity of the tent's slope at $\rho = \rho_w$ should be satisfied, giving an equation for $C_w$ according to Eqs. (15) and (48)

$$C_w = \frac{1}{\rho_w\sqrt{-\alpha}}\sqrt{\frac{\tilde{\psi}_w}{1-\tilde{\psi}_w}} \tag{60}$$

This problem containing multiple regions is then largely simplified (see Appendix D), which is to solve analytical Eqs. (57-60) for $\rho_b$ and $\rho_w$ with the prescribed center height of the tent $W_0$ and interfacial shear traction $T$. We find $\sqrt{-\alpha}W_0 \sim f(\rho_w)$ from Eqs. (59) and (60) and $\alpha T \sim g(\rho_b, \rho_w)$ from Eq. (57), which again enable the composite parameter $T/W_0^2$ to select $\rho_b$ and $\rho_w$.

## 7. Parametric studies based on far-from-threshold modeling

With the analytical FFT modeling, we are able to elucidate how the size of the buckled and wrinkled region evolves with the controlling composite parameter. It is worth noting that in FFT modeling, buckling instabilities take place and $\rho_b$ characterizes the extent of the buckled region by the size of the zero-$N_{\theta\theta}$ region; in NT modeling, instabilities are suppressed and $\rho_c$ represents the supported region where sliding radially inward occurs (i.e. $u < 0$). The extent of the buckled region (i.e. $\rho_b$ in FFT modeling) is directly accessible to AFM-based topographical characterizations; the sheet sliding around a tent accompanies radial tension and hoop compression – both of them vary radially, making $\rho_c$ in NT modeling accessible to Raman spectroscopy (Kitt et al., 2013; Wang et al., 2017c).

### 7.1. Extent of the buckled and wrinkled region

The $\rho_b - T/W_0^2$ and $\rho_w - T/W_0^2$ relations are plotted in Fig. 10a and b, respectively. As expected, like the size of the compression zone in the NT modeling, the extent of both buckled ($\rho_b$) and wrinkled ($1-\rho_w$) region increases in the FFT modeling as the composite parameter $T/W_0^2$ decreases. A key difference is that the formation of wrinkling and buckling requires a critical $T/W_0^2$ ( $\approx 0.43$), below which the buckled region appears and grows. The critical $T/W_0^2$ for the onset of instabilities results from Poisson's effect: a material circle (e.g. at the edge of the tent) is likely to wrinkle/buckle only when its inward shrinkage caused by the sliding overwhelms the lateral shrinkage caused by the radial tension. This critical value thus vanishes as the Poisson's ratio goes to zero.

### 7.2. NT and FFT modeling

It is natural to compare FFT with NT modeling regarding how $\rho_c$ evolves (Fig. 10a) as both types of modeling characterize $\rho = \rho_c$ by the position where the stresses decay to zero (neglecting the pretension and finite size of the sheet). We find that these two types of modeling give close $\rho_c - T/W_0^2$ prediction when $\rho_c < 3$ (the difference is within 20%), implying that the formation of buckling and wrinkling causes only a small perturbation to the stress state of a tent under such condition. However, the difference becomes increasingly significant as $\rho_c$ grows (in particular, it grows faster in the FFT modeling).

Besides, the spatial distribution of the hoop compression, $\bar{\Delta}$, (i.e. the shortened perimeter of a material circle) is intrinsically different between NT and FFT modeling. We have shown the scaling $\bar{\Delta} \sim \rho^{-1}$ in the analysis of NT modeling

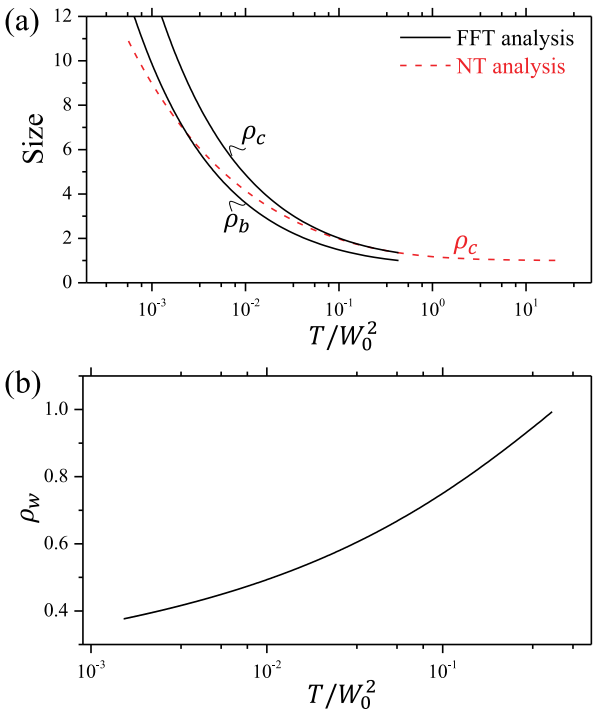


**Fig. 10.** (a) The dependency on $T/W_0^2$ of the extent of the buckled region $\rho_b$ (black solid curve, predicted by FFT analysis) and the size of the compression zone $\rho_c$ (black solid curve predicted by FFT analysis and red dashed curve predicted by NT analysis). (b) The dependency on $T/W_0^2$ of the extent of the wrinkled region $\rho_w$ in the suspended region of the tent (predicted by FFT analysis).

(Section 5) when the deformation is large, or the interfacial shear traction is small. In FFT modeling, the hoop compression is calculated from Eq. (55) that allows the hoop compressive stress to be relaxed by buckling,

$$\bar{\Delta} = -2\pi\tilde{u} = \pi T\left[\rho_b^2 \ln\frac{\rho_b}{\rho} + \frac{1}{2}\rho^2 - \frac{1}{2}\rho_b^2 + 2C_N \ln\frac{\rho_b}{\rho} + \frac{(1-\nu)(\rho_c-\rho_b)^2(\rho_c+2\rho_b)}{3\rho_b}\right]. \tag{61}$$

We plot $\bar{\Delta}$ as a function of $\rho$ in Fig. 11a for tents subject to different center heights and interfacial shear tractions. Clearly, the $\bar{\Delta} \sim \rho^{-1}$ relation breaks down (see solid and dashed curves). In addition, we find that the buckling instability brings more slip and hence, a larger hoop compression compared with the results in the NT modeling under the same loading condition. The physical interpretation is that the formation of the buckle delamination in the supported region makes the sheet (and its interface) less resistive to the inward sliding. We may also draw this conclusion by considering the shortened perimeter of the material circle at the edge of the tent, $\bar{\Delta}_1$ in Fig. 11b, where $\bar{\Delta}_1/W_0^2$ depends on a single parameter, $T/W_0^2$. Based on the analysis of NT modeling in Section 5, we also expect three additional governing parameters: $T_{pre}/W_0^2$, $\rho_{out}$, and $\rho_{in}$ in this FFT modeling when the pretension, the sheet's finite size, and the pillar's finite radius are taken into account. Here, we focus on the effect of the pillar's radius because of its particular uses in the mechanical metrology of interfacial shear traction and the design of pillar-poked tents that will be discussed in Section 8.

### 7.3. Finite pillar radius

We still consider the exemplary case where the radial displacement is fixed at the edge of the pillar. Using the same technique as outlined in Section 5.4, we show exact analytical solutions based on the FFT modeling in Appendix E. Similarly, two governing parameters appear in the FFT modeling: the radius of the pillar $\rho_{in}$ and the combined parameter $T/W_0^2$. We then show the dependency of the extent of the buckled region and wrinkled region on these two governing parameters in Fig. 12. To be consistent with Fig. 8, we focus on the domain $0.001 \leq \rho_{in} \leq 0.25$. The results as $\rho_{in} \to 0$ can recover those obtained by assuming a point force in Fig. 10 and the upper limit of $\rho_{in}$ also avoids $\rho_w < \rho_{in}$ (Fig. 12). Note that the blank regime in Fig. 12 covers the conditions under which instabilities are prohibited, and hence the nonzero radius of a pillar essentially facilitates the onset of instabilities. In general, tents poked by sharper pillars feature a shorter extent of the buckled and wrinkled region. However, non-monotonic behavior arises for $\rho_w$ in the bottom right corner of the contour plot in Fig. 12b. It would be interesting to clarify how the growth of the wrinkled region benefits from the pillar early yet becomes suppressed by the pillar when the wrinkle gets close to it as well as how the system behaves after the wrinkle comes into contact with the pillar in a future study.

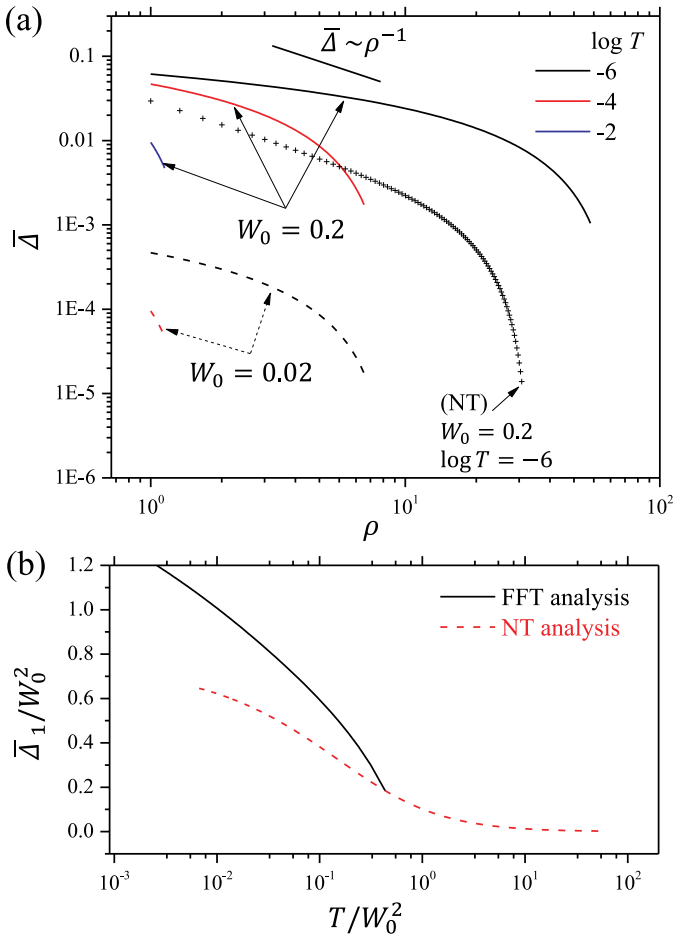


**Fig. 11.** (a) Hoop compressive displacement along the radial direction for various interfacial shear tractions. Solid curves denote tents with a center height $W_0 = 0.2$ while dashed curves denote $W_0 = 0.02$. The markers are from NT modeling in Fig. 5a. (b) The dependency on $T/W_0^2$ of the compressive displacement at the edge of the tent. The red dashed curve is from NT modeling in Fig. 5c.

## 8. Implications for 2D material applications

Having characterized buckles around the 2D material tent and modeled the tent with a sliding boundary analytically, we conclude by highlighting the implications of our results for 2D-material-based applications.

### *8.1. Estimation of interface adhesion*

In the nanoscale regime, the interactions between the 2D material and its substrate become relatively significant such that the performance of 2D-material–based devices relies heavily on the mechanical behaviors of interfaces Geim and Grigorieva, 2013; Neto et al., 2009). This fact has motivated extensive efforts to understand the mechanics of 2D material interfaces, especially adhesion and friction (Akinwande et al., 2017; Akinwande et al., 2014; Bunch and Dunn, 2012; Lloyd et al., 2017; Zhang et al., 2017; Zong et al., 2010). In Section 3.1, we pointed out that the crest curvature of the buckles can be used to estimate the interface adhesion between the 2D material and its substrate after identifying the content (i.e., gas or liquid) trapped inside the buckle. Plugging our measurements in Fig. 2c into Eqs. (4) and ((5), the extracted adhesion energy between the monolayer CVD-grown $MoS_2$ and $Al_2O_3$ is ~1.3 mJ/m$^2$ by taking the content as gas and the bending stiffness as 10 eV (Fig. 13a) (Androulidakis et al., 2018). If we assume that the buckles are filled with water such that $\gamma_l = 72$ mJ/m$^2$, $\theta_s = 36^\circ$, and $\theta_m = 69^\circ$ (Kozbial et al., 2015; Rafiee et al., 2012; Santos et al., 2003), Eq. (6) offers a more reasonable adhesion value of ~ 85.3 mJ/m$^2$, which is comparable with many adhesion values reported in the literature (Deng et al., 2017; Lloyd et al., 2017; Sanchez et al., 2018).

We have claimed that the water-filled buckle model could give a more reasonable adhesion value (comparable previous reports) than the gas model. The reason is that the former considers essentially three interfaces (water-membrane, water-substrate, and membrane-substrate) such that the wetting properties of the system will contribute to the extracted value of the membrane-substrate adhesion. However, so far there is no solid evidence for the presence of water trapped inside

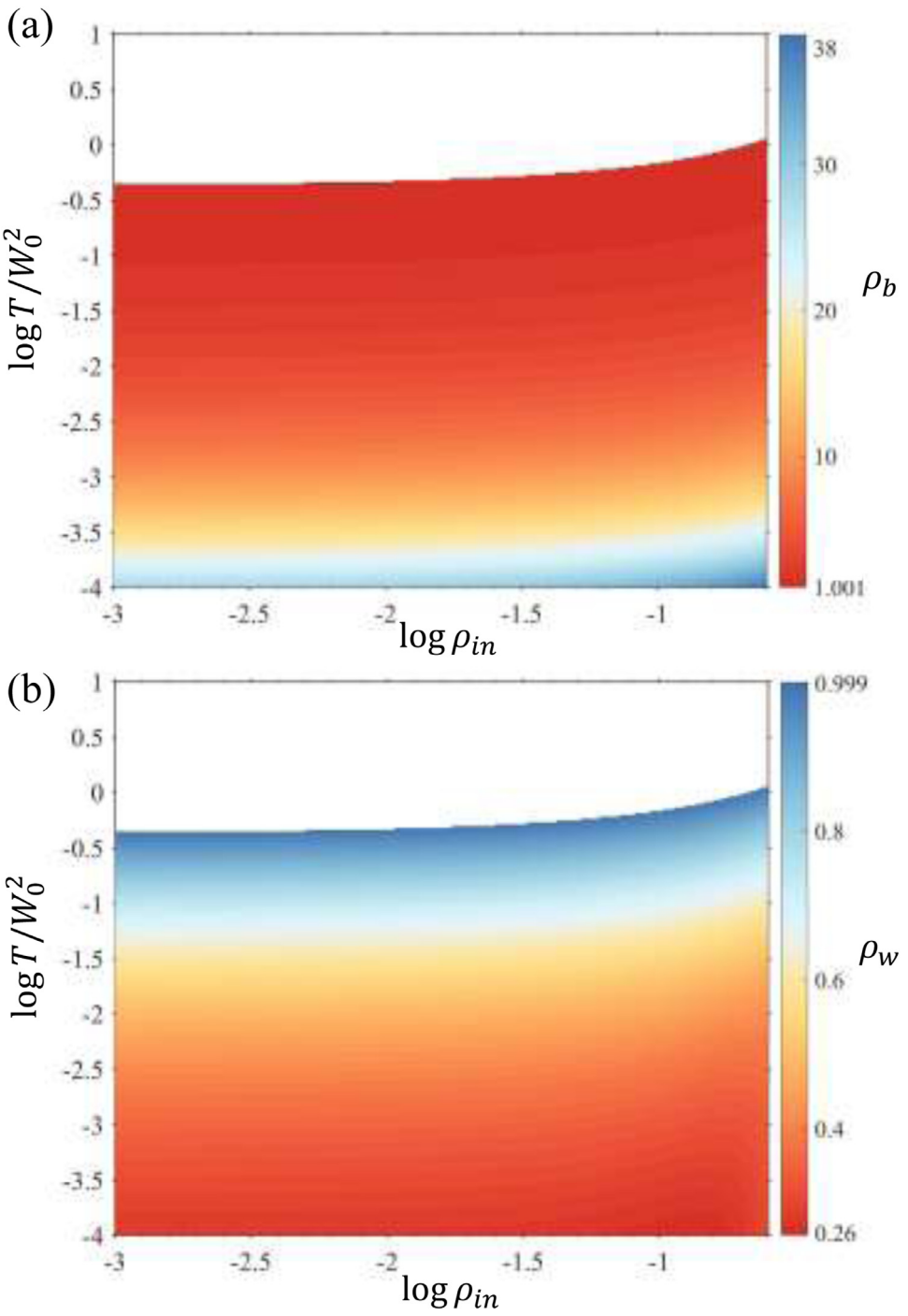


**Fig. 12.** Contour plots for the extent of the buckled region $\rho_b$ outside the tent (a) and the extent of the wrinkled region $\rho_w$ inside the tent (b) as a function of two governing parameters: $\rho_{in}$ and $T/W_0^2$.

the buckle through the SEM image in Fig. 13b shows likely liquid fringes near the edge of the tent (the darkish region near the white circle). The authors are working on characterizations of the trapped chemical components. It is expected that the detailed trapped substance contains both water and hydrocarbon that are readily absorbed in the 2D material-substrate interface (Khestanova et al., 2016), thus affecting the surface tension of the liquid, contact angle, and the extracted adhesion energy in Eq. (6). Besides, the mixed-mode adhesive interactions between the membrane and the substrate are not considered in this work. The above-mentioned adhesion is more rigorously called adherence (Boijoux et al., 2017; Faou et al., 2015; Hutchinson and Suo, 1991). However, the difference between adhesion and adherence in our system may be small due to the

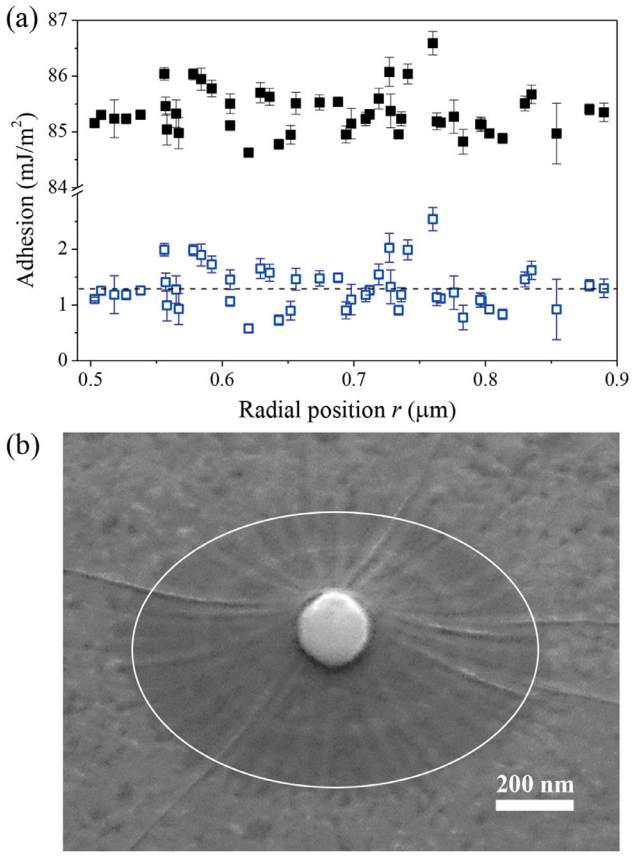


**Fig. 13.** (a) The estimated adhesion energy between CVD-grown monolayer $MoS_2$ and the $Al_2O_3$ substrate. This estimation is enabled by measuring the buckle profiles at different radial locations, which are offered in Fig. 3c. Blue markers are based on gas-filled buckles and solid markers are based on water-filled buckles. (b) The SEM image of the monolayer $MoS_2$ tent in Fig. 2a. The solid white circle highlights the edge of the tent.

facts that (i) the bending may dominate the deformation, and (ii) the interfacial shear traction is typically much weaker than normal traction as the interface is adhered by pure van der Waals (vdW) forces and 2D materials are atomically smooth. It would be interesting to examine the exact phase angle of mode-mix in this buckled configuration (Faou et al., 2015; Hutchinson and Suo, 1991), particularly with the consideration of the frictional features of the vdW interface (Ruffini et al., 2012a; Ruffini et al., 2012b).

### *8.2. Estimation of interface friction (FFT)*

Our present analysis relates the size of the compression zone (in NT) and the extent of the buckled and wrinkled region (in FFT) to four governing parameters: $T/W_0^2$, $T_{pre}/W_0^2$, $\rho_{out}$ and $\rho_{in}$. Experimentally, the effect of a sheet's finite size can be neglected, the tent height and the pillar radius can be accessible through AFM-based characterizations, while the force terms, i.e., interfacial shear traction and pretension, are relatively elusive. The pretension was extensively used as a fitting parameter in indentation tests and found to be less than ~ 0.4 N/m, i.e., $T_{pre} \sim 10^{-3}$ for graphene (Lee et al., 2008). However, the exact pretension varies heavily with materials, substrate, and transfer processes, and even appears to be negative (residual compression). Herein, we neglect the pretension effect such that we are able to estimate the interfacial shear traction via experimentally accessible parameters, including $\rho_b$, $\rho_{in}$, and $W_0$. It is worth noting that the pretension may be caused by surface tension at the outer edge of the membrane, epitaxial growth, thermal expansion and so on, which would modify such estimation (Dai et al., 2019a; Davidovitch et al., 2019). Experimentally, mapping of Raman bands may shed light on the level of the pretension but uncertainties are nontrivial due to the so-called doping effect from the substrate (Dai et al., 2019a).

We first focus on a CVD-grown monolayer $MoS_2$ tent. From its AFM height and amplitude image in Fig. 14a and b, we see both suspended, wrinkled region and supported, buckled region. We then assume that such instabilities can relax the hoop compressive stress in this atomically thin sheet such that our analytical FFT results in Section 7.3 can be leveraged directly. We measure the $W_0$ of this monolayer $MoS_2$ tent from its AFM height image and determine the tent radius by line-scans across the tent center as well as the ratio of pillar radius to tent radius ($\rho_{in}$ ~ 0.10). The tent's $\rho_b$ is simply estimated to be

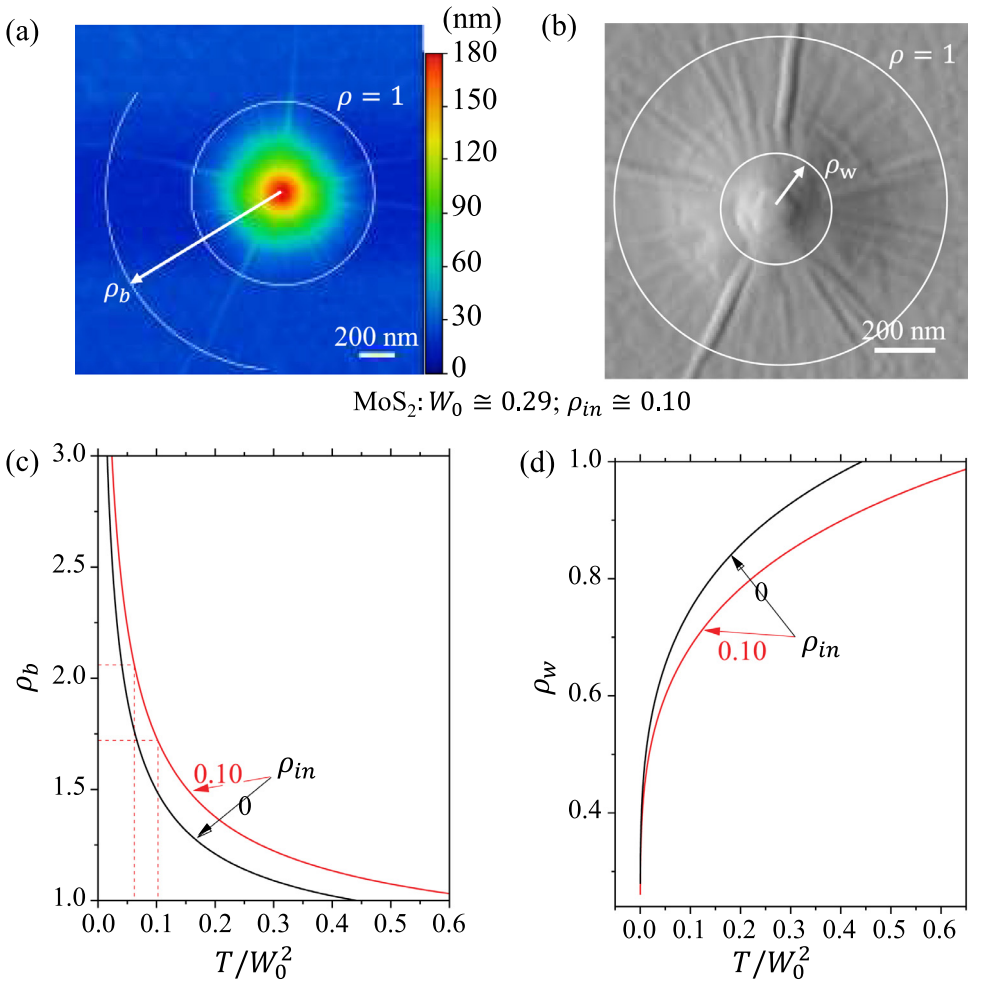


**Fig. 14.** AFM height (a) and amplitude (b) images of a monolayer $MoS_2$ tent, based on which $\rho_{in}$, $W_0$, $\rho_b$ and $\rho_w$ are extracted. The extent of the buckled region (c) and wrinkled region (d) depends on the interface shear traction $T$, the height of the tent $W_0$, and the radius of the pillar $\rho_{in}$. (b) is from Dai et al., 2018.

1.89 ± 0.17 through the location beyond which the buckles disappear (Fig. 14a) and, similarly, the tent's $\rho_w$ is found to be 0.35 ± 0.04 (Fig. 14b).

We plot the master $\rho_b \sim T/W_0^2$ curve for the specific $\rho_{in}$ in Fig. 14c. Plugging the geometrical parameters obtained above into the master curve leads to shear traction ranging from 1.7 to 2.9 MPa for the CVD-grown monolayer $MoS_2$ on $Al_2O_3$. However, our criterion that buckle delamination occurs in the supported region whenever the sheet is under compressive stress may cause errors in predicting the extent of the buckled region. The errors mainly come from the fact that the onset of buckle delamination of a sheet typically needs a nontrivial compressive strain (Vella et al., 2009) because of adhesion. Therefore, our criterion may underdetermine the extent of the buckled region and hence overestimate the traction. We also plot the master curve for the extent of the wrinkled region in Fig. 14d, plug the measured $\rho_w$ into it, and find a much weaker interfacial shear traction (~0.04 MPa). The huge inconsistency between $\rho_w$-based and $\rho b$-based estimations may be a result of the complexity in real experimental fabrications: the sheet is transferred with a pre-existing nanoparticle on the substrate, and the complicated contact occurs spontaneously. Our model is idealized for the situation that the center height of the tent is loaded quasi-statically, which calls for further controlled indentation experiments (possibly at larger scales) for validations.

### *8.3. Estimation of the interface friction (NT)*

We then move on to a relatively thick 2D flake, i.e. the ~15-layer graphene tent in Fig. 15. For this multilayer sample, the hoop compressive stress in the supported region may not be completely relaxed, and we then prefer to apply the NT analysis developed in Section 5.4 though the difference between FFT and NT analysis here could be minor since $\rho_c < 2$. More appropriate modeling might be achieved by considering the wrinkling instability in the suspended region of the tent

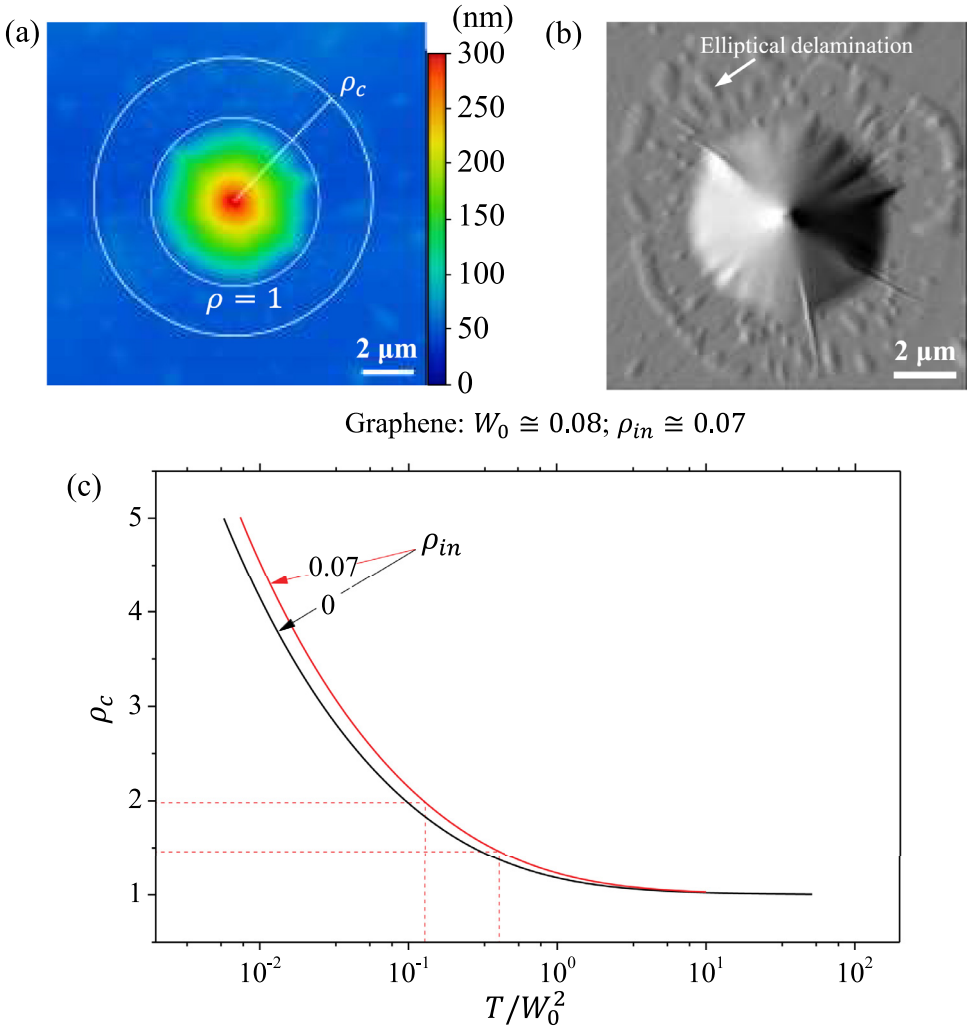


**Fig. 15.** AFM height (a) and amplitude (b) images of a ~15-layer graphene tent, based on which $\rho_{in}$, $W_0$, and $\rho_c$ are extracted. (c) The radius of the compression zone outside the tent depends on the interface shear traction $T$, the height of the tent $W_0$, and the radius of the pillar $\rho_{in}$. (b) is from Dai et al., 2018.

but neglecting the buckle or the buckle-caused stress relaxation in the supported region (we expect that the results should lie in between FFT and NT limits and the difference could be negligible for small $\rho_c$). We find an obvious coffee-ring-like domain in the supported region (see the AFM amplitude image in Fig. 15b). Inside this domain, the local delamination (labeled by the arrow) takes elliptical shapes with the long axis along the radial direction of the tent. Similar features have been observed recently in thin-film-capped droplets when an anisotropic stretch is applied to the thin film (Schulman and Dalnoki-Veress, 2018). In our case, the anisotropy within this coffee-ring-like domain should arise from the local hoop compression and radial tension, i.e. $N_{rr} > N_{\theta\theta}$, which are indeed caused by the inward sliding of the sheet ($u < 0$). We therefore approximately extract the corresponding $\rho_c = 1.72 \pm 0.26$ by the outer radius of this domain.

From the AFM height image of the multilayer graphene tent, we extract $W_0$ (~0.08) and $\rho_{in}$ (~0.07). The master $\rho_c \sim T/W_0^2$ curves for this specific $\rho_{in}$ is plotted in Fig. 15c based on NT modeling. Plugging these geometrical parameters into the master curve leads to shear traction ranging from 0.9 to 5.6 MPa for the exfoliated multilayer graphene on $SiO_2$. This result shows quantitative agreement with the shear traction, also called interfacial shear stress, which was measured to be 1-3 MPa for monolayer graphene on $SiO_2$ via bulging tests of drumhead specimens (Kitt et al., 2013; Wang et al., 2017a). The relatively large uncertainty for the multilayer graphene sample comes from the uncertainty in both $\rho_c$ and the number of layers (see Section 2, Fig. 16).

### *8.4. Guidelines for fabricating arrays of 2D material tents*

Recently, arrays of micro-tents became a popular strategy for the periodic strain engineering of 2D materials due to their self-sustainability and designability. A typical puzzle when designing arrays of 2D material tents comes from the dimensions

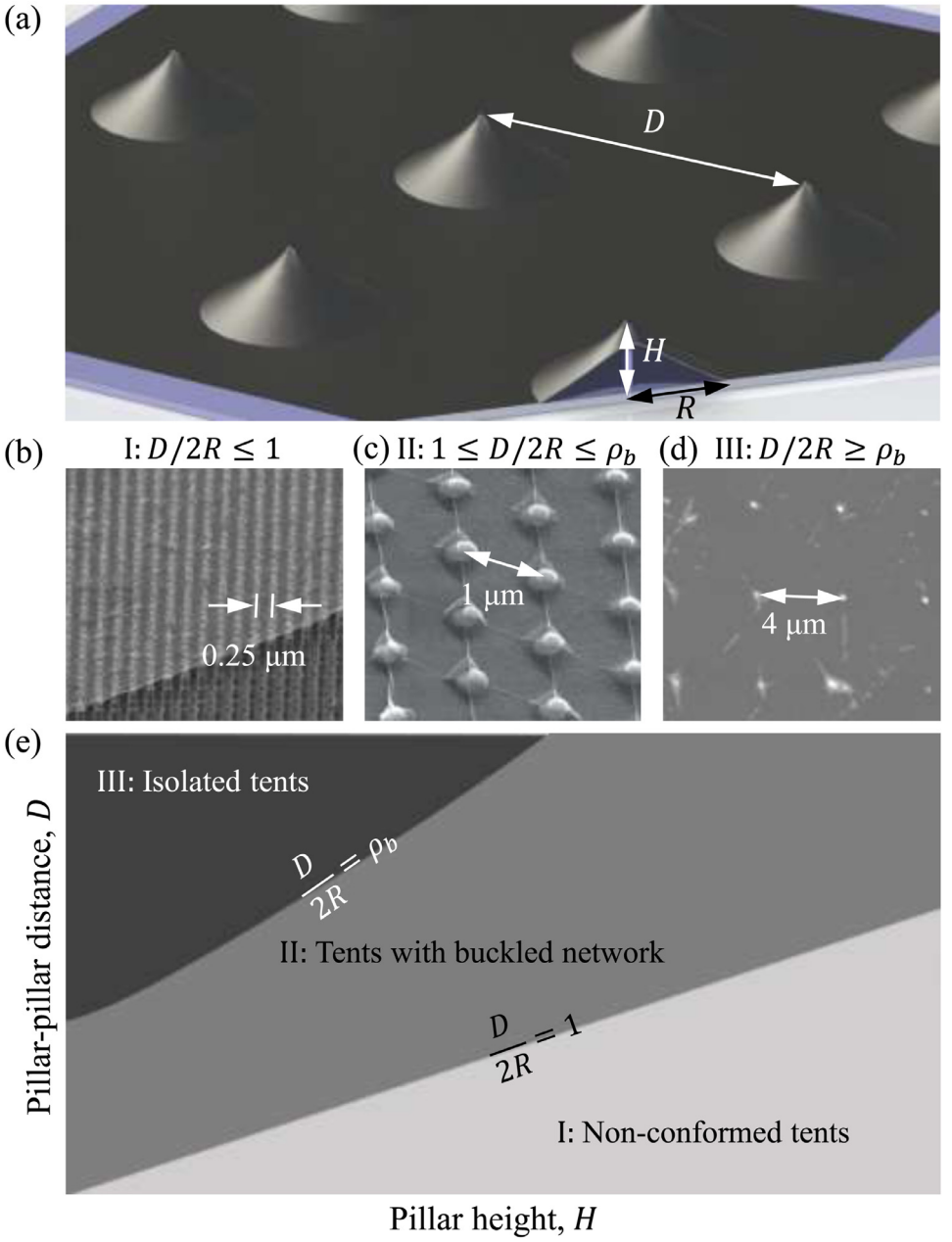


**Fig. 16.** (a) Schematic of an array of 2D material tents. (b) SEM image of CVD-grown monolayer graphene on silicon pillars (Reserbat-Plantey et al., 2014). (c) SEM image of CVD-grown monolayer graphene on lift-off resist nanopillars (Tomori et al., 2011). (c) AFM image of the topography of an exfoliated monolayer $WSe_2$ flake on top of negative resist nanopillars (Branny et al., 2017). (e) A Phase diagram of three configurations of 2D material tent arrays.

of the supporting micro/nanopillars. Though the sharpness of pillar tips is limited by the fabrication resolution, the pillar height $H$ and the pillar-pillar distance $D$ are relatively easy to control (Fig. 11a). However, improper design, such as $D \leq 2R$, may exclude the formation of tents (Fig. 11b); insufficient pillar-pillar distance, such as $2R \leq D \leq 2R_b$, may cause a network of buckles between tents (Fig. 11c); isolated tents require $D \geq 2R_b$ (Fig. 11d), which have been used as strain-engineered arrays of quantum emitters in applications (Branny et al., 2017).

Chopin *et al.* and Dai *et al.* have shown a linear relation between $R$ and $H$, i.e. $H/R \sim (\Delta\gamma/E_{2D})^{1/4}$, in thin membrane tent and the prefactors at two limits (i.e. $T \to \infty$ and $T \to 0$) were derived (Chopin et al., 2008; Dai et al., 2018) . Our results in Sections 5 and 7 further provide exact solutions to the nonlinear relation between $R_b/R$ (i.e. $\rho_b$) and $T/W_0^2$ ($W_0 = H/R$) as well as how such relation is affected by the radius of pillars. In other words, by knowing the elastic properties of the 2D material as well as the adhesion and friction properties of the 2D material-substrate interface, the configurations in Fig.

11b–11d can be designedly avoided or achieved by tuning the pillar-pillar distance, the pillar radius, and the pillar height. Furthermore, we suggest the formation of buckles may be suppressed by introducing pretension in this system (and *vice versa*). We hope that these quantitative understandings would lead to the deterministic design of arrays of 2D material tents in the future.

## 9. Conclusion

In this article, we present experimental observations on the radial buckles formed around 2D material tents and found an interesting characteristic length for the hoop-direction curvature of the buckle crests. A simple 1D model is adopted to show how the buckle shape relates to the material properties and the interface adhesion properties. The dependence of the buckle profile on the radial position further suggests that the interface sliding outside the tent may be the origin of hoop compression and buckle delamination. We establish analytical models for cases as simple as tents subjected to a point load at the center, zero shear traction at the interface, and zero pretension on the periphery all the way to tents with finite pillar size, finite pretension as well as finite flake size. Two types of modeling (i.e. NT and FFT modeling) accounting for none and complete compression relaxation are presented and may provide the upper and lower limits for this instability problem, respectively. Several governing composite parameters have been found for each case analytically by which the design of arrays of 2D material tents could be guided in a deterministic way. Furthermore, our theoretical analysis shows that the simple geometrical characterization of these buckles might be utilized for the adhesion and friction metrology of the 2D material-substrate interface.

## Declaration of Competing Interest

The authors declare that they have no known competing financial interests or personal relationships that could have appeared to influence the work reported in this paper.

## Acknowledgements

This work is supported by the NSF Division of Civil, Mechanical and Manufacturing Innovation (CMMI) under Grant No. 1351875 and the CNS Catalyst Grant at the University of Texas at Austin. Z.D. acknowledges the Warren A. and Alice L. Meyer Endowed Scholarship in Engineering, Eric Baker Becker III Memorial Graduate Scholarship, and UT Austin Graduate Continuing Fellowship. We also thank an anonymous referee for detailed, critical comments that helped improve our manuscript regarding the FFT modeling.

## Appendix A. Pretension (NT)

We enforce the continuity of radial stress and displacement at $\rho = 1$,

$$\Phi'\left(1^-\right) = \Phi'\left(1^+\right) \text{ and } \Phi''\left(1^-\right) - \nu\Phi'\left(1^-\right) = \Phi''\left(1^+\right) - \nu\Phi'\left(1^+\right), \tag{A1}$$

which lead to

$$\tilde{\psi}_1 = -\alpha\left(T_{pre} + b\right) \tag{A2}$$

and

$$\frac{\mathrm{d}\tilde{\psi}}{\mathrm{d}\eta}|_{\eta=1} = -\alpha T_{pre}. \tag{A3}$$

The continuity of displacement in Eq. (A3), together with Eq. (26), can give an equation for the constant $\alpha$

$$-\alpha T_{pre} = \frac{\bar{F}(-\alpha)^{3/2}}{4\pi}\sqrt{\frac{1-\tilde{\psi}_1}{\tilde{\psi}_1}}. \tag{A4}$$

We can eliminate the point force in Eq. (A4) by Eq. (29),

$$\alpha\left(T_{pre}, \tilde{\psi}_1\right) = \frac{1}{T_{pre}}\left[1 - \tilde{\psi}_1 - \sqrt{\frac{1-\tilde{\psi}_1}{\tilde{\psi}_1}}\tan^{-1}\sqrt{\frac{\tilde{\psi}_1}{\left(1-\tilde{\psi}_1\right)}}\right]. \tag{A5}$$

If we relate $\alpha$ to the center height of the tent $W_0$ by Eq. (37), it is readily found that the constant $\tilde{\psi}_1$ only rely on a combined parameter, $T_{pre}/W_0^2$ . Also, the continuity of radial stress in Eq. (A2) indicates that $b/T_{pre}$ is a function of $\tilde{\psi}_1$ or $T_{pre}/W_0^2$ by

$$\frac{T_{pre}}{b+T_{pre}} = 1 - \frac{1}{\tilde{\psi}_1} + \sqrt{\frac{1-\tilde{\psi}_1}{\tilde{\psi}_1^3}}\tan^{-1}\sqrt{\frac{\tilde{\psi}_1}{1-\tilde{\psi}_1}}. \tag{A6}$$

Finally, the size of the compression zone can be determined by Eq. (42)

$$\rho_c^2 = \frac{1+\nu}{1-\nu}\frac{b}{T_{pre}}, \tag{A7}$$

which implies $\rho_c \sim \rho_c(T_{pre}/W_0^2)$.

## Appendix B. Finite sheet size (NT)

The zero radial stress in Eq. (43) gives that

$$A + B = -\frac{C}{\rho_{out}^2} + \frac{2+\nu}{3}T\rho_{out}. \tag{B1}$$

The continuity conditions of radius stress and displacement in Eq. (30) hold and can lead to

$$\tilde{\psi}_1 = -\alpha\left[\left(1-\frac{1}{\rho_{out}^2}\right)C + \frac{2+\nu}{3}T(\rho_{out}-1)\right] \tag{B2}$$

and

$$\frac{\mathrm{d}\tilde{\psi}}{\mathrm{d}\eta}|_{\eta=1} = -\alpha\left(-\frac{1}{\rho_{out}^2}C + \frac{2+\nu}{3}T\rho_{out} - \frac{1+\nu}{2}T\right). \tag{B3}$$

Still utilizing the intermediate parameter $\tilde{\psi}_1$ in Eqs. (26) and (29), Eq. (B3) can give an equation for $\alpha$

$$-\alpha\left(-\frac{1}{\rho_{out}^2}C + \frac{2+\nu}{3}T\rho_{out} - \frac{1+\nu}{2}T\right) = -1 + \tilde{\psi}_1 + \sqrt{\frac{1-\tilde{\psi}_1}{\tilde{\psi}_1}}\tan^{-1}\sqrt{\frac{\tilde{\psi}_1}{1-\tilde{\psi}_1}}. \tag{B4}$$

We can further eliminate $\alpha$ by Eq. (B2) that provides an expression for the $C/T \sim \tilde{\psi}_1$ relation

$$\frac{-6C/T + 2(2+\nu)\rho_{out}^3 - 3(1+\nu)\rho_{out}^2}{6\left(\rho_{out}^2-1\right)C/T + 2(2+\nu)(\rho_{out}-1)\rho_{out}^2} = 1 - \frac{1}{\tilde{\psi}_1} + \sqrt{\frac{1-\tilde{\psi}_1}{\tilde{\psi}_1^3}}\tan^{-1}\sqrt{\frac{\tilde{\psi}_1}{1-\tilde{\psi}_1}}. \tag{B5}$$

We may also eliminate $\alpha$ in a different way, that is combining Eqs. (B2) and (37)

$$\tilde{\psi}_1 = \frac{4T}{W_0^2}\left[\left(1-\frac{1}{\rho_{out}^2}\right)\frac{C}{T} + \frac{2+\nu}{3}(\rho_{out}-1)\right]\left[\tan^{-1}\sqrt{\frac{\tilde{\psi}_1}{1-\tilde{\psi}_1}}\right]^2. \tag{B6}$$

Eqs. (B5) and (B6) indicates that $C/T$ is a function of the combined parameter $T/W_0^2$ and the geometrical parameter $\rho_{out}\,(>1)$.

## Appendix C. Finite pillar radius (NT)

When the pillar radius is finite, we lose the condition of $\tilde{\psi}(0) = 0$ in Eq. (28). Instead, the integration of Eq. (26) in this case brings a constant term

$$\frac{\bar{F}\sqrt{(-\alpha)^3}}{4\pi}\eta = -\sqrt{\tilde{\psi}\left(1-\tilde{\psi}\right)} + \tan^{-1}\sqrt{\frac{\tilde{\psi}}{1-\tilde{\psi}}} + C_{pillar}. \tag{C1}$$

However, this constant can be eliminated by considering the values of $\tilde{\psi}$ at $\rho = \rho_{in}$ and $\rho = 1$,

$$\frac{\bar{F}\sqrt{(-\alpha)^3}}{4\pi}\left(1-\rho_{in}^2\right) = -\sqrt{\tilde{\psi}_1\left(1-\tilde{\psi}_1\right)} + \sqrt{\tilde{\psi}_{in}\left(1-\tilde{\psi}_{in}\right)} + \tan^{-1}\sqrt{\frac{\tilde{\psi}_1}{1-\tilde{\psi}_1}} - \tan^{-1}\sqrt{\frac{\tilde{\psi}_{in}}{1-\tilde{\psi}_{in}}}. \tag{C2}$$

The $\bar{F}\sqrt{(-\alpha)^3}$ can be related to the intermediate parameter $\tilde{\psi}_{in}$ by Eq. (26) and the condition of fixed displacement at the edge of the tip in Eq. (46),

$$\frac{\bar{F}\sqrt{(-\alpha)^3}}{4\pi} = \frac{1+\nu}{2}\rho_{in}^{-2}\sqrt{\frac{\tilde{\psi}_{in}^3}{1-\tilde{\psi}_{in}}}. \tag{C3}$$

Then Eq. (C2) can be written as

$$\frac{1+\nu}{2}\sqrt{\frac{\tilde{\psi}_{in}^3}{1-\tilde{\psi}_{in}}}\left(\frac{1}{\rho_{in}^2} - 1\right) = -\sqrt{\tilde{\psi}_1\left(1-\tilde{\psi}_1\right)} + \sqrt{\tilde{\psi}_{in}\left(1-\tilde{\psi}_{in}\right)} + \tan^{-1}\sqrt{\frac{\tilde{\psi}_1}{1-\tilde{\psi}_1}} - \tan^{-1}\sqrt{\frac{\tilde{\psi}_{in}}{1-\tilde{\psi}_{in}}}. \tag{C4}$$

The continuity of displacement at the edge of the tent, i.e. Eq. (33), still requires

$$-\alpha T\frac{1+\nu}{2}(\rho_c-1)=\frac{\bar{F}(-\alpha)^{3/2}}{4\pi}\sqrt{\frac{1-\tilde{\psi}_1}{\tilde{\psi}_1}}. \tag{C5}$$

By combining Eqs. (C4), (C5), and (31) for the continuity of radial stress, we eliminate $\bar{F}$ and $\alpha$:

$$\frac{6\rho_{in}^2(\rho_c-1)}{3(1+\nu)\rho_c+(1-\nu)\rho_c^3-2(2+\nu)}=\sqrt{\frac{\tilde{\psi}_{in}^3\left(1-\tilde{\psi}_1\right)}{\tilde{\psi}_1^3\left(1-\tilde{\psi}_{in}\right)}}. \tag{C6}$$

As we aim to relate to the size of the compression zone $\rho_c$ to the height of the tent $W_0$, the integration domain is from $\rho_{in}$ to 1 in Eq. (36) such that

$$W_0=\frac{-\bar{F}\alpha}{4\pi}\int_{\tilde{\psi}_{in}}^{\tilde{\psi}_1}\frac{d\tilde{\psi}}{\tilde{\psi}\sqrt{\tilde{\psi}'}}=\frac{2}{\sqrt{-\alpha}}\left[\tan^{-1}\sqrt{\frac{\tilde{\psi}_1}{1-\tilde{\psi}_1}}-\tan^{-1}\sqrt{\frac{\tilde{\psi}_{in}}{1-\tilde{\psi}_{in}}}\right], \tag{C7}$$

where Eq. (26) was used for the analytical solution. Again, using Eqs. (C7) and (31) can cancel out $\alpha$ and lead to

$$\tilde{\psi}_1\left[\tan^{-1}\sqrt{\frac{\tilde{\psi}_1}{1-\tilde{\psi}_1}}-\tan^{-1}\sqrt{\frac{\tilde{\psi}_{in}}{1-\tilde{\psi}_{in}}}\right]^{-2}=\frac{4T}{W_0^2}\left(\frac{1+\nu}{2}\rho_c+\frac{1-\nu}{6}\rho_c^3-\frac{2+\nu}{3}\right). \tag{C8}$$

Now, $\tilde{\psi}_{in}$, $\tilde{\psi}_1$, and $\rho_c$ can be analytically solved by Eqs. (C4), (C6), and (C8) that only depend on two parameters – they are the size of the tip, $\rho_{in}$, and the combined parameter, $T/W_0^2$.

## Appendix D. The composite parameter (FFT)

Eq. (54) is solved based on the continuity of the hoop and radial stresses. Particularly, in the unbuckled, supported domain $[\rho_b,\ \rho_c]$, Eqs. (19)–(21) hold; and at the inner boundary of this domain, the hoop stress is released to be zero, which leads to

$$\rho_b=\frac{1-\nu+\sqrt{9+6\nu-15\nu^2}}{4+8\nu}\rho_c \tag{D1}$$

and

$$\frac{N_{rr}(\rho_b)}{E_{2D}}=T\left(-\frac{2+\nu}{3}\rho_b-\frac{\nu-1}{6}\rho_c^3\rho_b{}^{-2}+\frac{1+\nu}{2}\rho_c\right). \tag{D2}$$

We highlight the fast and easy implementation of our analytical solutions in calculating how the extent of wrinkles in the suspended region and buckles in the supported region evolves. Essentially, $\tilde{\psi}_w=0.6965$ is an independent constant and the intermediate parameters $C_w$ and $\alpha$ can be eliminated by combining Eqs. (57), (58), and (60)

$$2\ln\rho_w+2\nu+\frac{1}{\rho_w}\frac{1-\rho_w}{1-\tilde{\psi}_w}=\frac{2\rho_b^2\ln\rho_b-\rho_b^2+1+4C_N\ln\rho_b-4C_v\rho_b\rho_o}{\rho_b^2-1+2C_N}, \tag{D3}$$

or Eqs. (57), (59), and (60)

$$\frac{W_0^2}{T}\frac{2\tilde{\psi}_w}{\rho_w\left(\rho_b^2-1\right)+2C_N\rho_w}=\left(\frac{1-\rho_w}{\rho_w}\sqrt{\frac{\tilde{\psi}_w}{1-\tilde{\psi}_w}}+2\tan^{-1}\sqrt{\frac{\tilde{\psi}_w}{1-\tilde{\psi}_w}}\right)^2, \tag{D4}$$

where the governing parameter $T/W_0^2$ appears.

## Appendix E. Finite pillar radius (FFT)

In this case, the unwrinkled domain becomes $\rho_{in}\le\rho\le\rho_w$ where $\rho_{in}<\rho_w$. The integration of Eq. (26) over this domain gives

$$\frac{\bar{F}\sqrt{(-\alpha)^3}}{4\pi}\eta=-\sqrt{\tilde{\psi}\left(1-\tilde{\psi}\right)}+\tan^{-1}\sqrt{\frac{\tilde{\psi}}{\left(1-\tilde{\psi}\right)}}+C_{pillar}. \tag{E1}$$

We eliminate the integration constant by considering boundary values of $\tilde{\psi}$ at $\rho=\rho_{in}$ and $\rho=\rho_w$,

$$\frac{\bar{F}\sqrt{(-\alpha)^3}}{4\pi}\left(\rho_w^2-\rho_{in}^2\right)=-\sqrt{\tilde{\psi}_w\left(1-\tilde{\psi}_w\right)}+\sqrt{\tilde{\psi}_{in}\left(1-\tilde{\psi}_{in}\right)}+\tan^{-1}\sqrt{\frac{\tilde{\psi}_w}{1-\tilde{\psi}_w}}-\tan^{-1}\sqrt{\frac{\tilde{\psi}_{in}}{1-\tilde{\psi}_{in}}}. \tag{E2}$$

The condition of fixed displacement at the edge of the tip in Eq. (C3) holds. Plugging it into Eq. (E2) can give

$$\frac{1+\nu}{2}\sqrt{\frac{\tilde{\psi}_{in}^3}{1-\tilde{\psi}_{in}}}\left(\frac{\rho_w^2}{\rho_{in}^2}-1\right)=-\sqrt{\tilde{\psi}_w\left(1-\tilde{\psi}_w\right)}+\sqrt{\tilde{\psi}_{in}\left(1-\tilde{\psi}_{in}\right)}+\tan^{-1}\sqrt{\frac{\tilde{\psi}_w}{1-\tilde{\psi}_w}}-\tan^{-1}\sqrt{\frac{\tilde{\psi}_{in}}{1-\tilde{\psi}_{in}}} \tag{E3}$$

and into the condition of zero hoop stress at $\rho=\rho_w$, i.e. Eq. (48), leads to

$$(1+\nu)\rho_{in}^{-2}\sqrt{\frac{\tilde{\psi}_{in}^3}{1-\tilde{\psi}_{in}}}=\rho_w^{-2}\sqrt{\frac{\tilde{\psi}_w^3}{1-\tilde{\psi}_w}}. \tag{E4}$$

We note that Eqs. (57), (58), and (60) still apply because they are based on the continuity conditions at $\rho=\rho_w$ and $\rho=1$. However, to obtain the center height of the tent, Eq. (59) needs to change its integration domain,

$$W_0=W(\rho_w)+\int_{\rho_w}^{\rho_{in}}\frac{-\bar{F}d\rho}{2\pi\,\Phi'}=C_w(1-\rho_w)+\frac{2}{\sqrt{-\alpha}}\left[\tan^{-1}\sqrt{\frac{\tilde{\psi}_w}{1-\tilde{\psi}_w}}-\tan^{-1}\sqrt{\frac{\tilde{\psi}_{in}}{1-\tilde{\psi}_{in}}}\right]. \tag{E5}$$

As a result, the controlling equations discussed in Appendix D are modified,

$$2\ln\rho_w+2\nu+\frac{1}{\rho_w}\,\frac{1-\rho_w}{1-\tilde{\psi}_w}=\frac{2\rho_b^2\ln\rho_b-\rho_b^2+1+4C_N\ln\rho_b-4C_\nu\rho_b\rho_o}{\rho_b^2-1+2C_N}, \tag{E6}$$

$$\frac{W_0^2}{T}\,\frac{2\tilde{\psi}_w}{\rho_w\left(\rho_b^2-1\right)+2C_N\rho_w}=\left(\frac{1-\rho_w}{\rho_w}\sqrt{\frac{\tilde{\psi}_w}{1-\tilde{\psi}_w}}+2\tan^{-1}\sqrt{\frac{\tilde{\psi}_w}{1-\tilde{\psi}_w}}-2\tan^{-1}\sqrt{\frac{\tilde{\psi}_{in}}{1-\tilde{\psi}_{in}}}\right)^2, \tag{E7}$$

With the prescribed $\rho_{in}$ and a given composite parameter $\frac{T}{W_0^2}$, Eqs. (E3), (E4), (E6), and (E7) complete the conditions to determine $\tilde{\psi}_{in}$, $\tilde{\psi}_w$, $\rho_w$, and $\rho_b$. When the pillar has a finite radius, $\tilde{\psi}_w$ is not necessary to be a constant.

## References


Akinwande, D., Brennan, C.J., Bunch, J.S., Egberts, P., Felts, J.R., Gao, H., Huang, R., Kim, J.-S., Li, T., Li, Y., Liechti, K.M., Lu, N., Park, H.S., Reed, E.J., Wang, P., Yakobson, B.I., Zhang, T., Zhang, Y.-W., Zhou, Y., Zhu, Y., 2017. A review on mechanics and mechanical properties of 2D materials—Graphene and beyond. Extreme Mech. Lett. 13, 42–77.

Akinwande, D., Petrone, N., Hone, J., 2014. Two-dimensional flexible nanoelectronics. Nat. Commun. 5, 5678.

Androulidakis, C., Zhang, K., Robertson, M., Tawfick, S.H., 2018. Tailoring the mechanical properties of 2D materials and heterostructures. 2D Mater. 5, 032005.

Aoyanagi, Y., Hure, J., Bico, J., Roman, B., 2010. Random blisters on stickers: metrology through defects. Soft Matter. 6, 5720–5728.

Audoly, B., Boudaoud, A., 2008. Buckling of a stiff film bound to a compliant substrate—Part I: formulation, linear stability of cylindrical patterns, secondary bifurcations. J. Mech. Phys. Solids 56, 2401–2421.

Bhatia, N.M., Nachbar, W., 1968. Finite indentation of an elastic membrane by a spherical indenter. Int. J. Nonlin. Mech. 3, 307–324.

Boijoux, R., Parry, G., Coupeau, C., 2018. Buckle depression as a signature of Young's modulus mismatch between a film and its substrate. Thin Solid Films 645, 379–382.

Boijoux, R., Parry, G., Faou, J.-Y., Coupeau, C., 2017. How soft substrates affect the buckling delamination of thin films through crack front sink-in. Appl. Phys. Lett. 110, 141602.

Box, F., O'Kiely, D., Kodio, O., Inizan, M., Castrejón-Pita, A.A., Vella, D., 2019. Dynamics of wrinkling in ultrathin elastic sheets. Proc. Natl. Acad. Sci. USA, 201905755 doi:10.1073/pnas.1905755116.

Branny, A., Kumar, S., Proux, R., Gerardot, B.D., 2017. Deterministic strain-induced arrays of quantum emitters in a two-dimensional semiconductor. Nat. Commun. 8, 15053.

Brennan, C.J., Ghosh, R., Koul, K., Banerjee, S.K., Lu, N., Yu, E.T., 2017. Out-of-plane electromechanical response of monolayer molybdenum disulfide measured by piezoresponse force microscopy. Nano Lett 17, 5464–5471.

Brennan, C.J., Nguyen, J., Yu, E.T., Lu, N.S., 2015. Interface Adhesion between 2D materials and elastomers measured by Buckle delaminations. Adv. Mater. Interfaces 2, 1500176.

Budrikis, Z., Sellerio, A.L., Bertalan, Z., Zapperi, S., 2015. Wrinkle motifs in thin films. Sci. Rep. 5, 8938.

Bunch, J.S., Dunn, M.L., 2012. Adhesion mechanics of graphene membranes. Solid State Commun. 152, 1359–1364.

Cao, G., Gao, H., 2019. Mechanical properties characterization of two-dimensional materials via nanoindentation experiments. Prog. Mater. Sci. 103, 558–595.

Chaste, J., Missaoui, A., Huang, S., Henck, H., Ben Aziza, Z., Ferlazzo, L., Balan, A., Johnson, A.T.C., Braive, R., Ouerghi, A., 2018. Intrinsic properties of suspended $MoS_2$ on $SiO_2$/Si pillar arrays for nanomechanics and optics. ACS Nano 12, 3235–3242.

Chopin, J., Vella, D., Boudaoud, A., 2008. The liquid blister test. Proc. Royal Soc. A 464, 2887–2906.

Dai, Z., Hou, Y., Sanchez, D.A., Wang, G., Brennan, C.J., Zhang, Z., Liu, L., Lu, N., 2018. Interface-governed deformation of nanobubbles and nanotents formed by two-dimensional materials. Phys. Rev. Lett. 121, 266101.

Dai, Z., Liu, L., Zhang, Z., 2019a. Strain engineering of 2D materials: issues and opportunities at the interface. Adv. Mater., 1805417.

Dai, Z., Wang, G., Liu, L., Hou, Y., Wei, Y., Zhang, Z., 2016. Mechanical behavior and properties of hydrogen bonded graphene/polymer nano-interfaces. Compos. Sci. Technol. 136, 1–9.

Dai, Z., Wang, G., Zheng, Z., Wang, Y., Zhang, S., Qi, X., Tan, P., Liu, L., Xu, Z., Li, Q., Cheng, Z., Zhang, Z., 2019b. Mechanical responses of boron-doped monolayer graphene. Carbon 147, 594–601.

Davidovitch, B., Schroll, R.D., Vella, D., Adda-Bedia, M., Cerda, E.A., 2011. Prototypical model for tensional wrinkling in thin sheets. Proc. Natl. Acad. Sci. USA 108, 18227–18232.

Davidovitch, B., Sun, Y., Grason, G.M., 2019. Geometrically incompatible confinement of solids. Proc. Natl. Acad. Sci. USA 116, 1483–1488.

Davidovitch, B., Vella, D., 2018. Partial wetting of thin solid sheets under tension. Soft Matter 14, 4913–4934.

Deng, S., Gao, E., Xu, Z., Berry, V., 2017. Adhesion energy of $MoS_2$ thin films on silicon-based substrates determined via the attributes of a single $MoS_2$ wrinkle. ACS Appl. Mater. Interfaces 9, 7812–7818.

Faou, J.-Y., Parry, G., Grachev, S., Barthel, E., 2015. Telephone cord buckles—a relation between wavelength and adhesion. J. Mech. Phys. Solids 75, 93–103.
Feng, J., Qian, X., Huang, C.-W., Li, J., 2012. Strain-engineered artificial atom as a broad-spectrum solar energy funnel. Nat. Photon. 6, 866–872.
Geim, A.K., Grigorieva, I.V., 2013. Van der Waals heterostructures. Nature 499, 419–425.
Gong, L., Kinloch, I.A., Young, R.J., Riaz, I., Jalil, R., Novoselov, K.S., 2010. Interfacial stress transfer in a graphene monolayer nanocomposite. Adv. Mater. 22, 2694–2697.
Guo, G., Zhu, Y., 2015. Cohesive-shear-lag modeling of interfacial stress transfer between a monolayer graphene and a polymer substrate. J. Appl. Mech. 82, 031005.
Haigh, S., Gholinia, A., Jalil, R., Romani, S., Britnell, L., Elias, D., Novoselov, K., Ponomarenko, L., Geim, A., Gorbachev, R., 2012. Cross-sectional imaging of individual layers and buried interfaces of graphene-based heterostructures and superlattices. Nat. Mater. 11, 764–767.
Huang, J., Juszkiewicz, M., De Jeu, W.H., Cerda, E., Emrick, T., Menon, N., Russell, T.P., 2007. Capillary wrinkling of floating thin polymer films. Science 317, 650–653.
Hutchinson, J.W., Suo, Z., 1991. Mixed mode cracking in layered materials. In: Advances in Applied Mechanics. Elsevier, pp. 63–191.
Israelachvili, J.N., 2011. Intermolecular and Surface Forces. Academic press.
Jiang, T., Huang, R., Zhu, Y., 2013. Interfacial sliding and buckling of monolayer graphene on a stretchable substrate. Adv. Funct. Mater. 24, 396–402.
Jiang, Y., Mao, J., Duan, J., Lai, X., Watanabe, K., Taniguchi, T., Andrei, E.Y., 2017. Visualizing strain-induced pseudomagnetic fields in graphene through an hBN magnifying glass. Nano Lett. 17, 2839–2843.
Jin, C., Davoodabadi, A., Li, J., Wang, Y., Singler, T., 2017. Spherical indentation of a freestanding circular membrane revisited: analytical solutions and experiments. J. Mech. Phys. Solids 100, 85–102.
Khestanova, E., Guinea, F., Fumagalli, L., Geim, A.K., Grigorieva, I.V., 2016. Universal shape and pressure inside bubbles appearing in van der Waals heterostructures. Nat. Commun. 7, 12587.
Kitt, A.L., Qi, Z., Rémi, S., Park, H.S., Swan, A.K., Goldberg, B.B., 2013. How graphene slides: Measurement and theory of strain-dependent frictional forces between graphene and $SiO_2$. Nano. Lett. 13, 2605–2610.
Klimov, N.N., Jung, S., Zhu, S., Li, T., Wright, C.A., Solares, S.D., Newell, D.B., Zhitenev, N.B., Stroscio, J.A., 2012. Electromechanical properties of graphene drumheads. Science 336, 1557–1561.
Koenig, S.P., Boddeti, N.G., Dunn, M.L., Bunch, J.S., 2011. Ultrastrong adhesion of graphene membranes. Nat. Nanotechnol. 6, 543–546.
Komaragiri, U., Begley, M., Simmonds, J., 2005. The mechanical response of freestanding circular elastic films under point and pressure loads. J. Appl. Mech. 72, 203–212.
Kozbial, A., Gong, X., Liu, H., Li, L., 2015. Understanding the intrinsic water wettability of molybdenum disulfide ($MoS_2$). Langmuir 31, 8429–8435.
Lee, C., Wei, X., Kysar, J.W., Hone, J., 2008. Measurement of the elastic properties and intrinsic strength of monolayer graphene. Science 321, 385–388.
Li, H., Contryman, A.W., Qian, X., Ardakani, S.M., Gong, Y., Wang, X., Weisse, J.M., Lee, C.H., Zhao, J., Ajayan, P.M., 2015. Optoelectronic crystal of artificial atoms in strain-textured molybdenum disulphide. Nat. Commun. 6, 7381.
Liu, Z., Yang, J., Grey, F., Liu, J.Z., Liu, Y., Wang, Y., Yang, Y., Cheng, Y., Zheng, Q., 2012. Observation of microscale superlubricity in graphite. Phys. Rev. Lett. 108, 205503.
Lloyd, D., Liu, X., Boddeti, N., Cantley, L., Long, R., Dunn, M.L., Bunch, J.S., 2017. Adhesion, stiffness, and instability in atomically thin $MoS_2$ bubbles. Nano Lett. 17, 5329–5334.
Lu, Q., Arroyo, M., Huang, R., 2009. Elastic bending modulus of monolayer graphene. J. Phys. D: Appl. Phys. 42, 102002.
Mansfield, E.H., 2005. The Bending and Stretching of Plates. Cambridge University Press.
Neto, A.C., Guinea, F., Peres, N., Novoselov, K., Geim, A., 2009. The electronic properties of graphene. Rev. Mod. Phys. 81, 109.
Palacios-Berraquero, C., Kara, D.M., Montblanch, A.R.-P., Barbone, M., Latawiec, P., Yoon, D., Ott, A.K., Loncar, M., Ferrari, A.C., Atatüre, M., 2017. Large-scale quantum-emitter arrays in atomically thin semiconductors. Nat. Commun. 8, 15093.
Parry, G., Colin, J., Coupeau, C., Foucher, F., Cimetière, A., Grilhé, J., 2005. Effect of substrate compliance on the global unilateral post-buckling of coatings: AFM observations and finite element calculations. Acta Mater. 53, 441–447.
Pizzocchero, F., Gammelgaard, L., Jessen, B.S., Caridad, J.M., Wang, L., Hone, J., Boggild, P., Booth, T.J., 2016. The hot pick-up technique for batch assembly of van der Waals heterostructures. Nat. Commun. 7, 11894.
Py, C., Reverdy, P., Doppler, L., Bico, J., Roman, B., Baroud, C.N., 2007. Capillary origami: spontaneous wrapping of a droplet with an elastic sheet. Phys. Rev. Lett. 98, 156103.
Rafiee, J., Mi, X., Gullapalli, H., Thomas, A.V., Yavari, F., Shi, Y., Ajayan, P.M., Koratkar, N.A., 2012. Wetting transparency of graphene. Nat. Mater. 11, 217–222.
Reserbat-Plantey, A., Kalita, D., Han, Z., Ferlazzo, L., Autier-Laurent, S., Komatsu, K., Li, C., Weil, R.L., Ralko, A., Marty, L.T., 2014. Strain superlattices and macroscale suspension of graphene induced by corrugated substrates. Nano Lett. 14, 5044–5051.
Ruffini, A., Durinck, J., Colin, J., Coupeau, C., Grilhé, J., 2012a. Effects of sliding on interface delamination during thin film buckling. Scripta Mater. 67, 157–160.
Ruffini, A., Durinck, J., Colin, J., Coupeau, C., Grilhé, J., 2012b. Gliding at interface during thin film buckling: a coupled atomistic/elastic approach. Acta Mater. 60, 1259–1267.
Sadd, M.H., 2009. Elasticity: Theory, Applications, and Numerics. Academic Press.
Sanchez, D.A., Dai, Z., Wang, P., Cantu-Chavez, A., Brennan, C.J., Huang, R., Lu, N., 2018. Mechanics of spontaneously formed nanoblisters trapped by transferred 2D crystals. Proc. Natl. Acad. Sci. USA 115, 7884–7889.
Santos, F.d.P., Campos, E.d., Costa, M., Melo, F.C.L., Honda, R.Y., Mota, R.P., 2003. Superficial modifications in $TiO_2$ and $Al_2O_3$ ceramics. Mater. Res. 6, 353–357.
Schroll, R., Adda-Bedia, M., Cerda, E., Huang, J., Menon, N., Russell, T., Toga, K., Vella, D., Davidovitch, B., 2013. Capillary deformations of bendable films. Phys. Rev. Lett. 111, 014301.
Schulman, R.D., Dalnoki-Veress, K., 2018. Droplets capped with an elastic film can be round, elliptical, or nearly square. Phys. Rev. Lett. 121, 248004.
Timoshenko, S.P., Gere, J.M., 2009. Theory of Elastic Stability. Courier Dover Publications.
Tomori, H., Kanda, A., Goto, H., Ootuka, Y., Tsukagoshi, K., Moriyama, S., Watanabe, E., Tsuya, D., 2011. Introducing nonuniform strain to graphene using dielectric nanopillars. Appl. Phys. Express 4, 075102.
Vella, D., 2019. Buffering by buckling as a route for elastic deformation. Nat. Rev. Phys. 1, 425–436.
Vella, D., Adda-Bedia, M., Cerda, E., 2010. Capillary wrinkling of elastic membranes. Soft Matter 6, 5778–5782.
Vella, D., Bico, J., Boudaoud, A., Roman, B., Reis, P.M., 2009. The macroscopic delamination of thin films from elastic substrates. Proc. Natl. Acad. Sci. USA 106, 10901–10906.
Vella, D., Davidovitch, B., 2017. Indentation metrology of clamped, ultra-thin elastic sheets. Soft Matter 13, 2264–2278.
Vella, D., Davidovitch, B., 2018. Regimes of wrinkling in an indented floating elastic sheet. Phys. Rev. E 98, 013003.
Vella, D., Huang, J., Menon, N., Russell, T.P., Davidovitch, B., 2015. Indentation of ultrathin elastic films and the emergence of asymptotic isometry. Phys. Rev. Lett. 114, 014301.
Wang, G., Dai, Z., Liu, L., Hu, H., Dai, Q., Zhang, Z., 2016. Tuning the interfacial mechanical behaviors of monolayer graphene/PMMA nanocomposites. ACS Appl. Mater. Interfaces 8, 22554–22562.
Wang, G., Dai, Z., Wang, Y., Tan, P., Liu, L., Xu, Z., Wei, Y., Huang, R., Zhang, Z., 2017a. Measuring interlayer shear stress in bilayer graphene. Phys. Rev. Lett. 119, 036101.
Wang, G., Dai, Z., Xiao, J., Feng, S., Weng, C., Liu, L., Xu, Z., Huang, R., Zhang, Z., 2019. Bending of multilayer van der Waals materials. Phys. Rev. Lett. 123, 116101.
Wang, G., Gao, E., Dai, Z., Liu, L., Xu, Z., Zhang, Z., 2017b. Degradation and recovery of graphene/polymer interfaces under cyclic mechanical loading. Compos. Sci. Technol. 149, 220–227.

Wang, G., Li, X., Wang, Y., Zheng, Z., Dai, Z., Qi, X., Liu, L., Cheng, Z., Xu, Z., Tan, P., 2017c. Interlayer coupling behaviors of boron doped multilayer graphene. J. Phys. Chem. C 121, 26034–26043.
Xu, Z., Zheng, Q., 2018. Micro-and nano-mechanics in China: A brief review of recent progress and perspectives. Sci. China Phys. Mech. Astron. 61, 074601.
Zhang, D.-B., Akatyeva, E., Dumitrică, T., 2011. Bending ultrathin graphene at the margins of continuum mechanics. Phys. Rev. Lett. 106, 255503.
Zhang, K., Arroyo, M., 2016. Coexistence of wrinkles and blisters in supported graphene. Extreme Mech. Lett. 14, 23–30.
Zhang, K., Tadmor, E.B., 2018. Structural and electron diffraction scaling of twisted graphene bilayers. J. Mech. Phys. Solids 112, 225–238.
Zhang, Q.T., Yin, H., 2018. Spontaneous buckling-driven periodic delamination of thin films on soft substrates under large compression. J. Mech. Phys. Solids 118, 40–57.
Zhang, Y., Liu, Q., Xu, B., 2017. Liquid-assisted, etching-free, mechanical peeling of 2D materials. Extreme Mech. Lett. 16, 33–40.
Zong, Z., Chen, C.-L., Dokmeci, M.R., Wan, K.-T., 2010. Direct measurement of graphene adhesion on silicon surface by intercalation of nanoparticles. J. Appl. Phys. 107, 026104.